Journal of Alloys and Compounds 1008 (2024) 176691

Contents lists available at ScienceDirect

Journal of Alloys and Compounds

journal homepage: www.elsevier.com/locate/jalcom

A fresh perspective to synthesizing and designing carbon/sulfur composite cathodes using supercritical CO_2 technology for advanced Li-S battery cathodes

Lakshmi Shiva Shankar [a], Samantha K. Samaniego Andrade [b], Krisztina László [b], Dóra Zalka [c,d], Péter B. Nagy [e], Márton Szabados [f], Zoltán Pászti [a], Katalin Balázsi [g], Zsolt Czigány [g], Levente Illés [g], Robert Kun [a,h,*]

[a] Institute of Materials and Environmental Chemistry, HUN-REN Research Centre for Natural Sciences, Magyar tudósok krt. 2, Budapest H-1117, Hungary
[b] Department of Physical Chemistry and Materials Science, Faculty of Chemical Technology and Biotechnology, Budapest University of Technology and Economics, Műegyetem rkp. 3., Budapest H-1111, Hungary
[c] Institute of Materials Research, Slovak Academy of Sciences, Watsonova 47, Košice 04001, Slovak Republic
[d] Faculty of Science, Institute of Physics, Pavol Jozef Šafárik University in Košice, Košice 041 80, Slovak Republic
[e] Department of Physical Chemistry and Materials Science, University of Szeged, Rerrich Bela ter 1, Szeged H-6720, Hungary
[f] Department of Organic Chemistry, University of Szeged, Dom ter 8, Szeged H-6720, Hungary
[g] Institute of Technical Physics and Materials Science, HUN-REN Center for Energy Research, Konkoly Thege Miklós út 29-33,, Budapest H-1121, Hungary
[h] Department of Chemical and Environmental Process Engineering, Faculty of Chemical Technology and Biotechnology, Budapest University of Technology and Economics, Műegyetem rkp. 3, Budapest H-1111, Hungary

ARTICLE INFO

Keywords:
Li-S battery
Supercritical CO_2
Surface chemistry
Thermal reduction
Polysulfides
Pore morphology

ABSTRACT

The morphology and surface chemistry of the sulfur host within lithium-sulfur (Li-S) batteries significantly influence the overall battery performance. To investigate this relationship, we employed a non-toxic heat treatment to produce reduced graphene oxide (rGO) with varying degrees of reduction, resulting in distinct surface chemistries. The physicochemical characteristics and electrochemical properties of four differently reduced GO samples and rGO/sulfur composite cathodes developed with supercritical CO_2 technology were examined. Our study established a clear correlation between the specific surface area and porosity of rGO and the electrochemical performance of the corresponding rGO/sulfur composite cathodes. Notably, rGO samples reduced at 350°C (rGO350) exhibited superior discharge capacity and long-term cycling stability compared to those reduced at higher temperatures. This performance enhancement can be attributed to the combination of high surface area, porosity, and an open morphology in rGO350. These findings underscore the importance of optimizing carbon chemistry, microstructure, and cathode synthesis strategies in Li-S batteries. By effectively controlling sulfur loading and distribution within the rGO network, we can enhance active material utilization, boost electronic conductivity, and ensure the long-term stability of rGO/sulfur composite cathodes. Our research suggests that SC-CO_2-assisted synthesis offers a promising approach for designing high-performance carbon/sulfur composite cathodes for Li-S batteries. This method provides a versatile platform for tailoring the rGO morphology and surface chemistry, optimizing battery performance. By carefully considering the interplay between these factors, we can unlock the full potential of Li-S batteries for various applications.

1. Introduction

The increasing demand for portable electronic devices has made developing innovative technologies for creating electrochemical energy storage systems crucial. Despite the widespread use of lithium-ion batteries, their energy density remains limited at the cell level, making them inadequate for next-generation electric vehicles (EVs) and smart-grid energy storage systems. Additionally, the high cost and toxicity of

* Corresponding author at: Institute of Materials and Environmental Chemistry, HUN-REN Research Centre for Natural Sciences, Magyar tudósok krt. 2, Budapest H-1117, Hungary.
E-mail address: kun.robert@ttk.hu (R. Kun).

https://doi.org/10.1016/j.jallcom.2024.176691
Received 1 June 2024; Received in revised form 22 September 2024; Accepted 24 September 2024
Available online 24 September 2024

materials like nickel and cobalt in these batteries hinder their broader application. Therefore, it is essential to explore advanced, less toxic battery systems with high energy density that utilize abundant raw materials and are environmentally friendly. Lithium-sulfur batteries hold immense potential for next-generation energy storage systems due to their high theoretical energy density and the natural abundance of sulfur. In the coming years, Li-S batteries could achieve practical energy densities of around 450–500 Wh/Kg at the cell level. With the integration of cost-effective and sustainable active materials, Li-S batteries will be more accessible and environmentally friendly for the consumer [1–6].

While lithium-sulfur batteries offer impressive theoretical energy density and affordability, they face critical challenges that hinder their performance. Key issues include the poor electrical and ionic conductivity of sulfur and lithium polysulfides (LiPS), the problematic shuttle effect of LiPS, significant volume expansion during cell reactions, and the formation of lithium dendrites. These problems drastically reduce the battery's efficiency and reduce its practical energy density. Addressing these challenges is crucial, and substantial research is focused on innovatively designing sulfur hosts to overcome these limitations [7–14].

Different types of pores are advantageous for improving specific capacity, rate capability, and cycling stability in sulfur-carbon composite cathodes [15–17]. Optimizing porous structures, which often feature exterior micropores and interior meso/macropores, can help mitigate these issues to some extent through hierarchical porous structure design. Remarkably, even similar carbon-sulfur composites exhibit different electrochemical performance. This implies that the pore synthesis method plays a critical role in enhancing battery performance through structural design optimization and synthesis technique advancements [18].

Functionalising the carbon matrix is another factor that improves the performance of sulfur-carbon composite cathodes. Nazar et al. [19] reported the detailed mechanism of the chemical interactions associated with the polysulfides, namely polar-polar interactions, Lewis acid-base interactions, and sulfur chain catenation [19]. Numerous studies have shown that carbon structures decorated with specific functional groups can reduce the shuttle effect, enhancing the cycle life of the Li-S battery system compared to non-functionalized or pristine carbon. Since carbon, a hydrophobic host, cannot efficiently adsorb and retain highly polar lithium polysulfides during extended cycling, attaching polar functional groups to the carbon network induces strong chemical interactions with sulfur and lithium polysulfides, restricting their dissolution and subsequent shuttling. This immobilization of sulfur and lithium polysulfides allows for maximum active material utilization, resulting in highly reversible and stable cells over prolonged cycling [20].

Through this work, we aim to combine these two aspects—porous structural features and the presence of functional groups—in the development of differently reduced graphene oxide using thermal treatment. A key feature of this study is that the rGO/sulfur composites are fabricated using supercritical carbon dioxide (SC-CO_2) technology. As reported in our previous work [21], this synthesis method has proven to be one of the best non-toxic, facile, and efficient strategies for homogeneously incorporating sulfur into the rGO matrix, resulting in composite cathodes with excellent electrochemical performance. To date, various conventional synthesis routes have been employed to prepare electrode-active materials for Li-S batteries. These routes include melt diffusion [22], chemical vapor deposition [23,24], solution infiltration [25,26], wet chemical processes involving soluble sulfur-containing compounds [27–30], and mechanical infusion such as ball milling [31]. Bonilla et al. recently described the impact of composite preparation on the electrochemical performance of Li-S batteries [32]. However, these traditional methods are associated with numerous drawbacks. They are time-consuming and require high temperatures and significant energy consumption. A few drawbacks of employing traditional synthesis techniques are: 1) Melt diffusion: Sulfur must be physically mixed with the host materials, but this does not guarantee homogeneity at the nanoscale. Additionally, melt diffusion requires a minimum temperature of 155°C. High diffusion resistance often leads to low production efficiency, significant energy waste from extended heating, and an uncontrollable sulfur coating on host materials. 2) Ball milling: Despite being effective for mixing and dispersing materials, ball milling may struggle to achieve uniform nanoscale dispersion of sulfur within the carbon host due to potential agglomeration. Furthermore, it is a time-consuming process. 3) Dissolution/recrystallization: Although less energy-intensive, this process does not guarantee homogeneous recrystallization, and controlling the process is difficult due to varying crystallization kinetics depending on the solvent. 4) Vacuum infiltration: This involves sophisticated sealing with expensive glass tubes that may frequently break, and it must be carried out at temperatures exceeding 300°C under vacuum. Scaling up this process is therefore challenging and costly. 5) Chemical vapour deposition: Controlling the morphology and structure of sulfur is difficult, and this method is not optimal on its own. It is often combined with melt diffusion for better results. Additionally, using toxic solvents like carbon disulfide, benzene, toluene, and cyclohexane in many methods poses environmental and safety risks. Additionally, these methods often fail to allow sulfur to penetrate the inner pores of the carbon framework, reducing sulfur utilization and leading to less efficient electrochemical performance.

These issues highlight the importance of developing a straightforward, environmentally friendly, and efficient technology to synthesize high-performance carbon-sulfur composite cathodes. When designing battery electrode materials, it is crucial that the solvents used are inert, non-toxic, environmentally benign, abundant, economically viable at scale, and available in high purity. Supercritical carbon dioxide (SC-CO_2) meets all these criteria, making it an excellent choice for preparing composite electrodes for Li-S batteries. SC-CO_2 transforms from a liquid into a supercritical fluid by raising the temperature and pressure above its critical limits (31.1°C and 7.4 MPa), possessing unique physical and chemical properties such as minimal surface tension. Its low and easily accessible critical parameters allow it to be used at moderate temperatures without generating hazardous organic residues. Moreover, SC-CO_2's density can be adjusted by varying the temperature and pressure, enabling it to dissolve non-polar or slightly polar molecules, like non-polar solvents like hexane. The solvation strength of SC-CO_2 can also be enhanced by adding small amounts of other solvents, such as alcohols. Compared to conventional synthesis routes, SC-CO_2 synthesis facilitates the preparation of ultrathin, uniform particles with good crystallinity. CO_2 is a green, safe, and abundant solvent, making upscaling of this synthesis technology easier. Due to its unique properties, SC-CO_2 is highly effective in synthesizing, modifying, and recycling battery components. It acts as an excellent foaming agent for creating porous structures that host electrodes, and its high permeability, diffusivity, and dissolving power allow it to transport active materials into inner pores, ensuring uniform distribution. SC-CO_2 is thus a 'super-solvent' for preparing composite cathodes for Li-S batteries.

In this work, graphene oxide is prepared using the conventional modified Hummers' method [33]. Graphene oxide (GO) comprises graphene sheets decorated mostly with epoxide and hydroxyl groups. However, due to the disruption of its sp^2 bonding networks, GO is an electrical insulator. Hence, to utilize the potential of GO in the Li-S battery cathode, GO should be reduced to rGO, which is highly conductive. Out of various reduction techniques, we adopted thermal reduction contrary to a chemical reduction involving harmful chemicals like hydrazine hydrate, dimethylhydrazine, hydroquinone, $NaBH_4$, etc. As reported in our previous work [21], the synergistic effect of physical confinement (by SC-CO_2) and chemical confinement (by polar functional groups attached to rGO) resulted in RGO/S composite cathodes with ultra-stable cycle life performance. However, we investigated the graphene oxide reduced only at a single temperature of 350 °C. Detailed characterization and electrochemical performance tests were conducted. As an extension, foreseeing the potential of reduced graphene oxide

systems, herein, we investigate the influence of GO reduction temperature on the surface chemistry of rGO (in terms of specific surface area and porosity), morphology as well as the changes in functional groups, especially oxygen-rich sites present in the reduced graphene oxide (rGO) host. The correlation between the structural changes of rGO and its electrochemical performance is evaluated. This study adds no external functionalization agents to the rGO backbone. Apart from non-toxicity, another significant benefit of using thermal reduction and structural control is the minimal synthesis time. In our study, the reduction time is less than 15 minutes. This means that reaction time is not a constraint when upscaling of this strategy. A comparative analysis is conducted on the physicochemical characteristics of differently reduced GO and their distinct electrochemical properties as a potential sulfur host in Li-S batteries. It was observed that compared to the rGO synthesized at higher temperatures (550 °C - 950 °C), the rGO synthesized at low temperatures (350 °C) exhibited the highest surface area, porosity, and most open porous morphology, making it the most suitable host for sulfur. The results obtained in this study divulge a potential opportunity to create the most appropriate sulfur host with low-temperature requirements.

2. Materials and methods

2.1. Synthesis of graphene oxide using a modified Hummers' method

The Hummers' and modified Hummer's methods are the most widely used chemical synthesis routes for GO. In this study, we used a modified Hummers' method, which involves both oxidation and exfoliation of graphite sheets owing to the thermal treatment of the feed suspension. In this process, 2 g graphite powder (SGA-20, 99.9 % carbon content) and 2 g $NaNO_3$ (Sigma Aldrich, 99 %) were added to 60 mL H_2SO_4 (Sigma Aldrich, 98 %) in a 1000 mL flask under gentle, continuous stirring. Subsequently, 6 g of potassium permanganate (Sigma Aldrich, 99 %) was added gradually to the suspension. The addition rate was carefully controlled to keep the reaction temperature below 15 °C. The mixture was then diluted with 60 mL of water and placed in an ice bath to cool completely. After cooling, the resulting mixture was treated with H_2O_2, yielding a bright yellow suspension. The mixture was then centrifuged with deionized water and dialyzed for several days to remove any ionic impurities. After dialysis, the GO was freeze-dried overnight to yield GO powder.

2.2. Thermal reduction of GO

The freeze-dried pristine GO was thermally reduced at four different temperatures: 230 °C, 350 °C, 550 °C, and 950 °C under a flowing nitrogen atmosphere for 20 minutes to obtain reduced GO (rGO) that can serve as sulfur host in the preparation of rGO/sulfur composite formation. The GO reduced at 230 °C, 350 °C, 550 °C, and 950 °C is denoted as rGO230, rGO350, rGO550, and rGO950, respectively.

2.3. Supercritical CO_2-assisted synthesis of rGO/sulfur composites

For the synthesis of the rGO/sulfur composites, 30 wt% of rGO (230,350, 550, and 950) and 70 wt% of elemental sulfur powder was mixed using an agate mortar for a few minutes and transferred into the high-pressure supercritical reactor. CO_2 (99.9 %) was pumped into the reactor, and the mixture was agitated at 350 RPM for 12 hours. The temperature and pressure during the supercritical infusion process were maintained at 30 °C and 150 bars, respectively. After the SC-CO_2-assisted reaction, the reactor was depressurized slowly by releasing the CO_2. The as-prepared rGO/sulfur composites were then collected from the reactor, denoted as rGO230-S-SCC, rGO350-S-SCC, rGO550-S-SCC, and rGO950-S-SCC.

2.4. Materials characterization

X-ray diffraction (XRD) patterns were obtained using PW3040/60 (Philips, Netherlands) X-ray diffractometer with a Cu-Ka radiation source ($\lambda = 1.5418$ Å; 40 kV acceleration voltage; Ni filter used as a beta-filter). Raman spectroscopy measurements were done on a Bruker Senterra II Raman microscope (Bruker Optics, Bremen, Germany) at 10 mW laser power level and 532 nm excitation wavelength. The normalized spectra were collected from 8 scans with 15 seconds of exposure time and 10x objective magnification. Nitrogen adsorption measurements at low temperatures (-196.15°C) were made using an automatic volumetric instrument- NOVA 2000e (Quantachrome, Boynton Beach, FL, USA) after a 24-hour degassing period at 110°C. The Brunauer-Emmett-Teller (BET) model was used to calculate the apparent surface area. The micropore volume V_{micro} was estimated using the Dubinin-Radushkevich (DR) model. The amount of vapor adsorbed at $p/p_0 = 0.94$ was used to determine the pore volume $V_{0.98}$, assuming that the adsorbed gas fills the pores as liquid. Before N_2 adsorption measurements, samples were evacuated at 110°C for 24 hours. The thermal behavior of the materials was characterized by thermogravimetric (TG) measurement (TA instruments Discovery TGA instrument) coupled with a mass spectrometer (MS, Hiden Analytical, HPR-20 EGA). The thermogravimeter was operated at a constant flow of Argon containing 10 % O_2 (60 mL/min) at a heating rate of 10 °C/min. For measurements, 20–30 mg of solids were placed in high-purity alpha-alumina crucibles. X-ray photoelectron spectroscopic (XPS) measurements were performed using an Omicron EA 125 electron spectrometer in the "Fixed Analyzer Transmission" mode with non-monochromatized Mg Kα (1253.6 eV) radiation with resolution around 1 eV. The energy scale of the electron spectrometer was calibrated according to the ISO 15472 standard. Scanning electron microscopy, coupled with Energy dispersive X-ray spectroscopy (SEM-EDS), was done using a Thermo Scientific Scios2 Dual Beam instrument equipped with an Oxford X-Max 20 energy dispersive X-ray spectrometer. The samples were fixed onto silicon wafers by using SEMGlu. The applied electron beam parameters for SEM imaging were 5 keV beam energy and 200 pA beam current. The electron beam parameters for X-ray mapping were 5 keV beam energy and 6.4 nA beam current. The Lamellae of the samples for transmission electron microscopy (TEM) were prepared by focused ion beam technique (FIB) using a Thermo Scientific Scios2 dual beam system. To minimize artifacts, two final polishing procedures were applied in FIB sample preparation: 5 kV and 48 pA and 2 kV 27 pA. The internal microstructure of the samples was analyzed under high-resolution TEM (TEM), energy dispersive spectroscopy (EDS), High-angle annular dark-field imaging (HAADF), and selected area electron diffraction (SAED) in a Cs corrected 200 kV Themis microscope (ThermoFisher).

2.5. Electrode preparation and half-cell assembly

The rGO/sulfur composites produced via supercritical reaction (rGO230-S-SCC, rGO350-S-SCC, rGO550-S-SCC and rGO950-S-SCC were mixed with conductive carbon black (Super C65, Imerys), and polyvinylidene fluoride (PVDF 99.9 %, Solvay), in a weight ratio of 80:10:10. Prior to mixing, the carbon black and PVDF were preheated to remove any moisture. The mixture was ball-milled for two hours, and then N-methyl-2-pyrrolidone (99.9 %, Sigma-Aldrich) was added as a solvent until the slurry achieved the desired consistency. The slurry was then spread onto copper foil using an automatic film applicator (BYK Gardner GmbH). The coated electrode film was initially dried in a Gravity Convection Oven at 55 °C for 30 minutes followed by vacuum drying at 60°C for 12 hours. The sulfur mass loading on each electrode was approximately 2.2 mg/cm^2. The dried cathode tape was punched into 12 mm discs using a disc cutter (Berg & Schmid GmbH). The cathode discs were then placed in the glove box's antechamber under evacuation for 24 hours prior to cell fabrication.

Coin-type cells (CR2032) were assembled inside the argon-filled

glovebox with lithium-metal foil (99.9 %, Sigma Aldrich) as the counter and reference electrode, Whatman glass fiber as the separator and 1 M Lithium bis(trifluoromethanesulfonyl)imide (LiTFSi: 99.95 %, Sigma Aldrich) in 1:1 vol ratio of 1,3-dioxolane (DOL: 99 %, Sigma Aldrich) and 1,2-dimethoxy ethane (DME: 99.5 %, Sigma Aldrich) as the electrolyte. The cells were assembled using an MTI MSK 110 manual crimping machine. The schematics for the entire cell fabrication process are shown in Fig. 1.

3. Results and discussions

3.1. Characterization of pristine reduced graphene oxide and the rGO/sulfur composite samples

3.1.1. Specific surface area and pore size distribution

Low-temperature nitrogen adsorption measurements were conducted to reveal the porous structure of the rGO and rGO-S-SCC sets of samples. According to the IUPAC classification, all the isotherms (Fig. 2a) are of type IV - type II and exhibit a hysteresis loop H3 [34]. The shape of the isotherms suggests an interconnected network of micro-, meso-, and macropores. The pore volume was estimated at $p/p_0 = 0.94$, corresponding to the pores not wider than 38 nm. The pyrolysis temperature of the rGO samples caused a systematic increase in surface area, pore volume, and micropore volume except for sample rGO350, which reached the maximum values for all three properties (Fig. 2a, Table 1). This might be due to the explosive thermal reduction of GO at around 300°C, which led to extra activation of rGO [35]. After infusing the rGO samples with sulfur, there was about a tenfold drop in the porous structure-related properties (Fig. 2b, Table 1).

The integral and differential pore size distribution curves from the adsorption branches of the rGO and rGO-S-SCC sets are shown in Fig. 2c-f. As no kernel is available for the sulfur-containing samples, we used the Barrett-Joyner-Halenda (BJH) model. Although this model is strictly valid in the 2–50 nm range, we present the differential curves on a wider scale for better visibility. A comparison of the corresponding integral distribution curves shows that the sulfur infusion affects the pores from the micro up to the macro-region. According to Figs. 2e and 2f, the micropores and most of the mesopores are almost filled with sulfur in the rGO230-S-SCC and rGO350-S-SCC composites, whereas only rGO950-S-SCC shows appreciable N_2 adsorption in the 2–50 nm range.

3.1.2. Structural analysis by powder X-ray Diffraction (XRD) and Raman spectroscopy

The phase structure of rGO230, rGO350, rGO550, and rGO950 was analysed using XRD. The diffractograms (Fig. 3a) show broad diffraction peaks assigned to (002) planes, indicating their amorphous nature. The feature at $2\theta = 24.5°$ corresponds to the stacking of graphene layers [36], while a weak feature at 42° indicates short-range order. A GO signal is still visible at $2\theta = 11.9°$, suggesting the coexistence of GO and rGO or incomplete GO reduction [37], possibly due to the shorter reduction time. The rGO samples consist of highly disordered graphene lamellae. The XRD analysis indicates that this range of reduction temperatures does not induce structural modifications in rGO.

To examine the structural changes in the rGO matrices after incorporating sulfur, the rGO/S composites were also analysed using XRD. Fig. 3b shows the X-ray diffractograms of the rGO230-S-SCC, rGO350-S-SCC, rGO550-S-SCC, and rGO950-S-SCC composites. The elemental sulfur diffraction peaks correspond to the characteristic peaks of orthorhombic alpha sulfur (JCPDS 00–001–0478). The distinct peaks of crystalline sulfur indicate the presence of sulfur within the rGO matrix.

The degree of graphitization of rGO230-S-SCC, rGO350-S-SCC, rGO550-S-SCC, and rGO950-S-SCC are determined by Raman spectroscopy analysis. From the investigation, all four rGO-S composite powders exhibited two broad peaks at 1350 cm^{-1} and 1580 cm^{-1}, corresponding to the defects of the sp^2 structure and the vibrations of the ordered graphene structure, respectively. Table 2 presents the Intensities and intensity ratios of D and G bands and full width at half maximum (FWHM) of the G bands collected from the Raman spectra of rGO230-S-SCC, rGO350-S-SCC, rGO550-S-SCC, and rGO950-S-SCC. The intensity ratio of these two peaks provides information about the ratio of sp^3 and sp^2 bonded carbon atoms in the graphene backbone. Upon the reduction, the number of sp^3-type atoms is expected to decrease due to the removal of oxygen-containing groups of graphene oxide. The FWHM of the G band is also proportional to the total number of defects of the graphene-like structure. The results show no significant differences in the composition of the reduced graphene oxide backbone. The minor difference in the obtained I_D/I_G arises from the number of randomly distributed defects. From the analysis, we can state that the reduction of

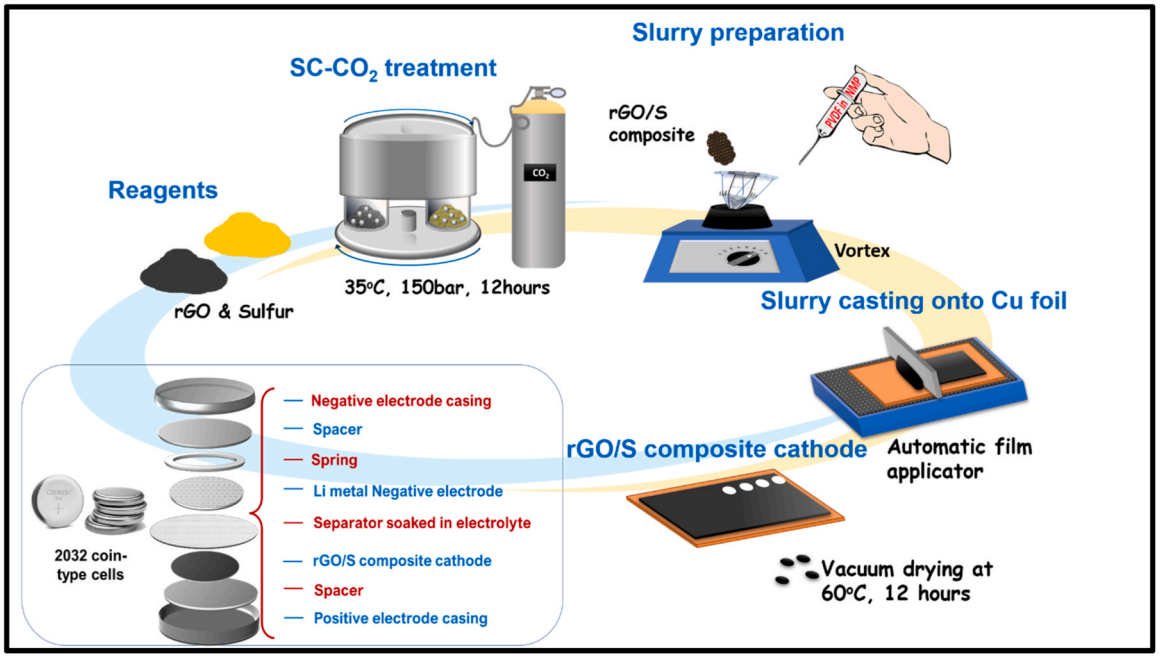

Fig. 1. Scheme of coin-type cell fabrication starting from raw materials.

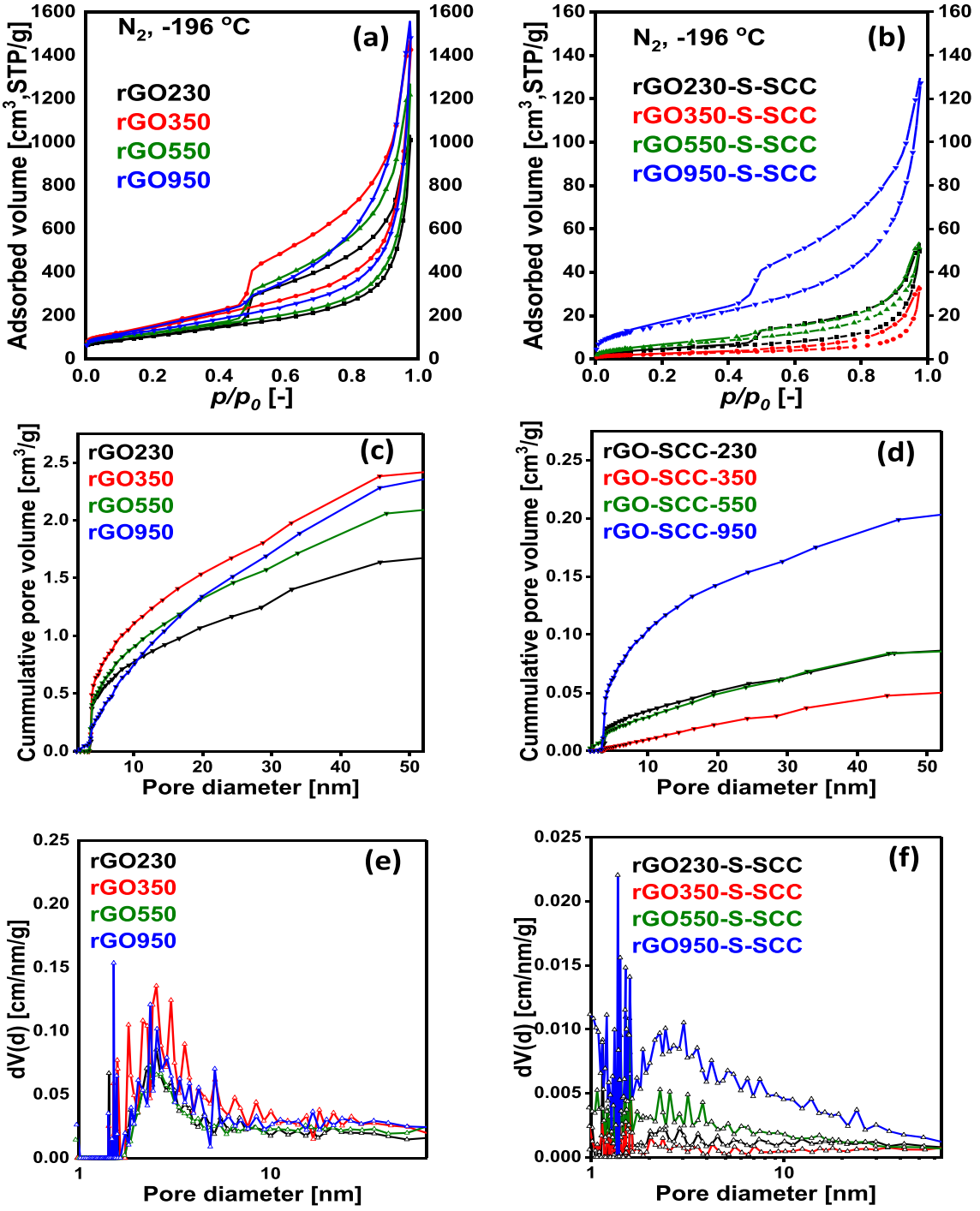

Fig. 2. Low temperature (-196 °C) N_2 adsorption-desorption isotherms of (a) heat-treated rGO and (b) sulfur-infused rGO samples (rGO-S-SCC). Pore size distribution curves of (c) heat-treated rGO and (d) sulfur-infused rGO (rGO-S-SCC) samples derived from the adsorption branches with the BJH model and the corresponding differential distributions (e- f).

GO in this temperature range (230°C-950°C) does not cause a considerable change in the crystal structure and degree of graphitization of the reduced graphene oxide phase of the composite samples.

3.1.3. Morphological analysis by scanning electron microscopy (SEM) coupled with energy dispersive spectroscopy (EDS) and high resolution-transmission electron microscopy (TEM)

Fig. 4 shows the morphology of the pristine sulfur, the four differently reduced rGO, and the rGO/sulfur composites analysed under SEM.

In this set of images, Fig. 4a shows the morphology of pristine sulfur used in this study, while Fig. 4(b–e) displays the pristine rGOs. Among these, rGO350 (Fig. 4c) exhibits an ultrathin, paper-like morphology with an open porous structure, folded regions, and wrinkles (as shown in the magnified image in Fig. 4c). In comparison, the other three images of rGO230, rGO550, and rGO950 (Figs. 4b, 4d, and 4e) show a higher propensity to form random aggregations besides having wrinkles and edges.

The non-aggregation tendency in rGO350, compared to the other rGOs, can be attributed to increased interlayer spaces, weakening the van der Waals forces between the layers [38]. This creates a larger space

Table 1
Porous characteristics from gas adsorption measurements*.

Sample	S_{BET} [m^2/g]	$V_{0.94}$ [cm^3/g]	$V_{micro\ DR}$ [cm^3/g]	V_{meso} [cm^3/g]
rGO230	398	0.879	0.137	0.742
rGO350	575	1.275	0.185	1.090
rGO550	436	0.976	0.159	0.817
rGO950	501	1.195	0.172	1.023
rGO230-S-SCC	17	0.044	0.006	0.038
rGO350-S-SCC	8	0.023	0.003	0.020
rGO550-S-SCC	24	0.053	0.008	0.045
rGO950-S-SCC	62	0.136	0.021	0.115

* S_{BET}: apparent surface area from BET model, $V_{0.94}$: the liquid equivalent of the gas adsorbed at $p/p_0 = 0.94$, $V_{micro\ DR}$: micropore volume from DR model. $V_{meso}=V_{0.94}-V_{micro}$.

to accommodate more sulfur particles within the rGO. Overall, the morphology of the graphene sheets indicates successful exfoliation, creating thin layers with high surface area and electrical conductivity, making them an ideal host for active sulfur nanoparticles. Fig. 4(f–i) show the SEM images of the rGO/sulfur composites. The SC-CO_2-assisted infusion process resulted in composite particles fragmenting into a platelet-like shape. EDS with overlapping maps of sulfur and carbon (Fig. 4j–m) shows the homogeneous spatial distribution of sulfur nanoparticles in the rGO framework, forming the rGO/sulfur nanocomposite. Among these, rGO350-S-SCC (Fig. 4k) displays the most even dispersion of sulfur nanoparticles in the rGO matrix.

For further insight into the detailed microstructure of the rGOs and the rGO/S composites with enhanced resolution, the samples rGO350 and rGO350-S-SCC were chosen and analyzed by TEM and selected area electron diffraction (SAED). To investigate the presence and distribution of sulfur in the rGO matrix, rGO350-S-SCC was analysed using energy dispersive spectroscopy (EDS), and the results are shown in Fig. 5(a-e). In the TEM images of rGO350 and rGO350-S-SCC, domains composed of graphitic layers can be observed. The interplanar distance (*d*) for the samples was determined by SAED analysis, and the SAED patterns are shown in Fig. 5(c-d). The interplanar distance (d) for the samples was determined by SAED analysis, and the patterns are shown in Fig. 5c–d. The interplanar distance of rGO350 (3.67 Å) increased to 3.75 Å after adding sulfur nanoparticles, indicating successful encapsulation of sulfur into the rGO backbone. The HAADF-EDS mapping of rGO350-S-SCC (Fig. 5e–g) confirms the uniform distribution of sulfur (yellow) without agglomeration in the porous rGO structure (red), demonstrating rGO's suitability as a host for sulfur and sulfur-lithium clusters formed during charge-discharge processes [39].

3.1.4. X-ray photoelectron spectroscopy (XPS)

X-ray photoelectron spectroscopy, a surface-sensitive quantitative spectroscopic technique, is utilized in this work to identify the surface composition and chemical states of the pristine rGO230, rGO350, rGO550, and rGO950.

Table 3 summarizes surface composition data. Apart from the expected C and O, minor quantities of N, S, Na, and Mn contaminants were detected, originating from the Hummers' method used to prepare GO. The net contaminant content in all samples was less than one atomic percent.

The different functional groups present in the rGO network were identified using the high-resolution C 1 s and O 1 s spectra of the samples. C 1 s spectra were modelled by a line shape for graphitic carbon (measured on an almost oxygen-free Super C65 carbon black reference sample) with additional peaks arising from different functional groups, while O 1 s spectra were deconvoluted based on literature examples [40]. A limitation of this approach is the overlap of the binding energy range of different bonding arrangements [40].

Fig. 6(a) shows the C1s spectra of the pristine rGO230, rGO350, rGO550, and rGO950, along with that of the carbon black reference. All spectra are dominated by the asymmetric line shape of graphitic carbon, located at 284.4 eV binding energy [41], indicating the significant surface reduction of GO even after the 230°C reduction treatment. Additional peaks needed for adequate fit indicated the presence of functional groups. According to the C 1 s spectra (or the composition data in Table 3), the functional group content of rGO230, rGO350, and rGO550 was identical; a higher reduction level was observed only in the case of rGO950. A small peak at 285.9 eV observed in the spectrum of all rGO samples was attributed to carbon singly bound to oxygen. This contribution is interpreted as C-OH groups or C-O-C-like arrangements, such as cyclic ethers at the edges of the graphene sheets or epoxide groups on the basal planes. Nevertheless, certain (especially isolated) carbonyl groups can also contribute to this peak. For heat treatments between 230 and 550°C, the estimated amount of these contributions was always around 10–11 % of the total carbon content, which decreased to 5 %

Table 2
The Intensities and intensity ratios of D and G bands, and full width at half maximum (FWHM) of the G bands collected from the Raman spectra of rGO230-S-SCC, rGO350-S-SCC, rGO550-S-SCC, and rGO950-S-SCC.

	rGO230-S-SCC	rGO350-S-SCC	rGO550-S-SCC	rGO950-S-SCC
ID	332.65	353.67	432	384.18
IG	359.50	381.42	477.48	377.82
I(D/G)	0.925	0.927	0.904	1.017
FWHM G	106.41	112.87	108.18	106.60

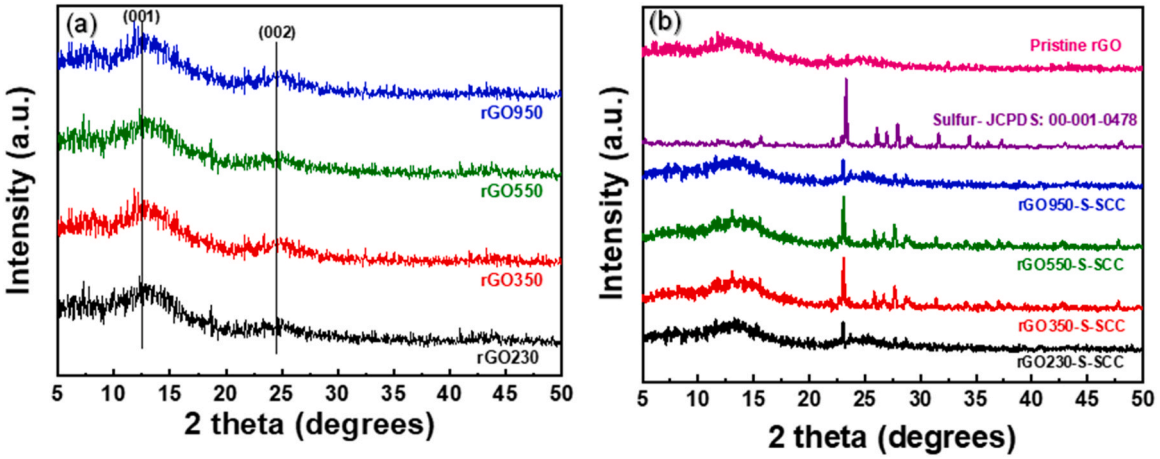

Fig. 3. XRD patterns of (a) rGO230, rGO350, rGO550 and rGO950, (b) rGO230-S-SCC, rGO350-S-SCC, rGO550-S-SCC and rGO950-S-SCC.

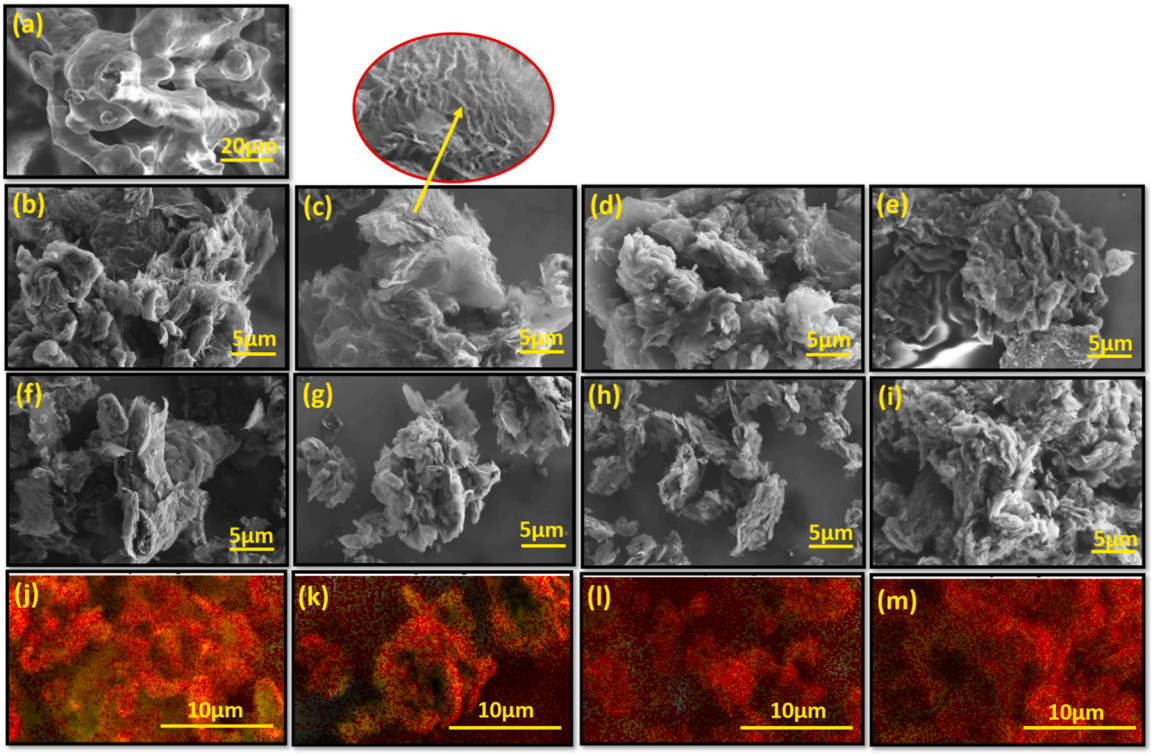

Fig. 4. SEM images of (a) Pristine sulfur; (b-e) rGO230, rGO350, rGO550, and rGO950 respectively; (f-i) rGO230-S-SCC, rGO350-S-SCC, rGO550-S-SCC, and rGO950-S-SCC respectively; (j-m) corresponding EDS layered/overlapping images of carbon and sulfur for rGO230-S-SCC, rGO350-S-SCC, rGO550-S-SCC, and rGO950-S-SCC respectively. The inset shows the area chosen for the elemental mapping. (The magnification of the sulfur image is presented at 1000* magnification to reveal the morphology with more clarity. All other images which are compared in the study are of the same magnification (5000*)).

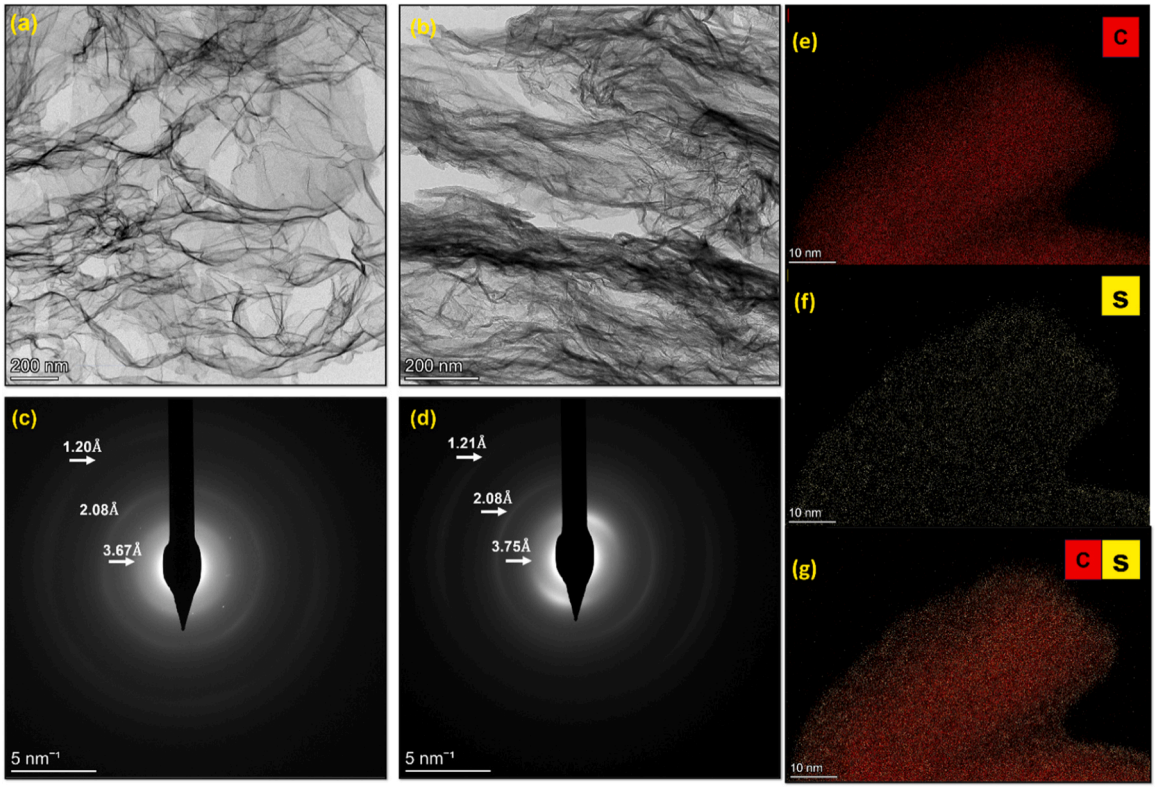

Fig. 5. TEM images of (a) rGO350 and (b) rGO350-S-SCC; (c-d) SAED patterns of rGO350 and rGO350-S-SCC, respectively; (e-f) EDS mapping of carbon and sulfur respectively; (g) combined carbon-sulfur EDS map of rGO350-S-SCC.

Table 3
Surface composition (atomic %) measured by XPS.

Sample	C	O	O / C	Net metal content
rGO230	86.6	11.8	0.136	0.90
rGO350	86.1	12.3	0.142	0.70
rGO550	85.8	12.6	0.146	1.00
rGO950	91.3	5.9	0.064	0.40

after reduction at 950°C. A higher binding energy component at 287.7–287.9 eV can be assigned to more highly oxidized carbon species such as carbonyls, carboxylic, or anhydride functionalities or carbon atoms bound to more than one oxygen atom in different configurations like lactones [42]. The relative amount of this type of contribution was always around 5 % of the total carbon content for the lower treatment temperatures and decreased to 2 % after annealing to 950°C.

Fig. 6(b) shows the O1s spectra of the pristine rGO230, rGO350, rGO550 and rGO950. The spectra are in tentative agreement with the assignments of the carbon signals. The lowest binding energy contribution was identified at around 530.2–530.3 eV and assigned to carbonyl groups at edge or basal plane positions. This peak accounted for roughly 20 % of the total oxygen content. The next component (around 20 % of the oxygen intensity) was found at 531.2–531.3 eV, which can still contain carbonyl-like contributions and signals from epoxide groups. The third, very intense peak (some 50 % of the total O content) at 533.3 eV can be assigned to –OH groups at edge positions or carboxylic groups, as well as to oxygens in C-O-C bonds in cyclic ethers or lactones. A fourth, relatively weak peak (5 %) at 535.3–535.4 eV may arise due to adsorbed moisture or C-O-C bonds at strongly oxidized edges of graphene sheets. The broad but relatively weak feature above 537 eV reflects an energy loss process due to the excitation of the aromatic electron system26,[40]. The line shape changes of the O 1 s peak were moderate throughout the annealing series; only a preferential loss of -OH/cyclic ether-like species was evident at the 950°C step. Similarly to the carbon spectra, the overall oxygen intensity also reflected the stability of the functional group structure up to 550°C, thus the oxygen-to-carbon (O/C) ratio of rGO230, rGO350, rGO550, and rGO950 did not show a monotonous trend.

Although chemical intuition would suggest gradual loss of functional groups after annealing at elevated temperatures, results of this study indicated that very few changes take place between 230°C-550°C and noticeable oxygen loss, along with rearrangement of the oxygen-containing groups start only after the heat treatment at 950°C. Literature [40,42] indicates qualitatively similar behavior. While GO exhibits a remarkably high level of functionalization with epoxide-like features as the most prevalent functional groups, they are reported to be largely eliminated or transformed after annealing to 300°C. After that, up to 500°C, relatively minor changes are observed, and the most important functional groups are lactones and cyclic ethers; the reported line shapes are close to those found on the present samples. Further annealing to higher temperatures seems to push the oxygen atoms toward the edges of the graphene sheets, resulting in highly oxidized edge regions without significant oxygen loss. Based on this comparison, the functional group structure of the present samples is relatively similar, dominated by C (=O)-O-C (lactone) and C-O-C (cyclic ether) - like features and some carbonyl groups.

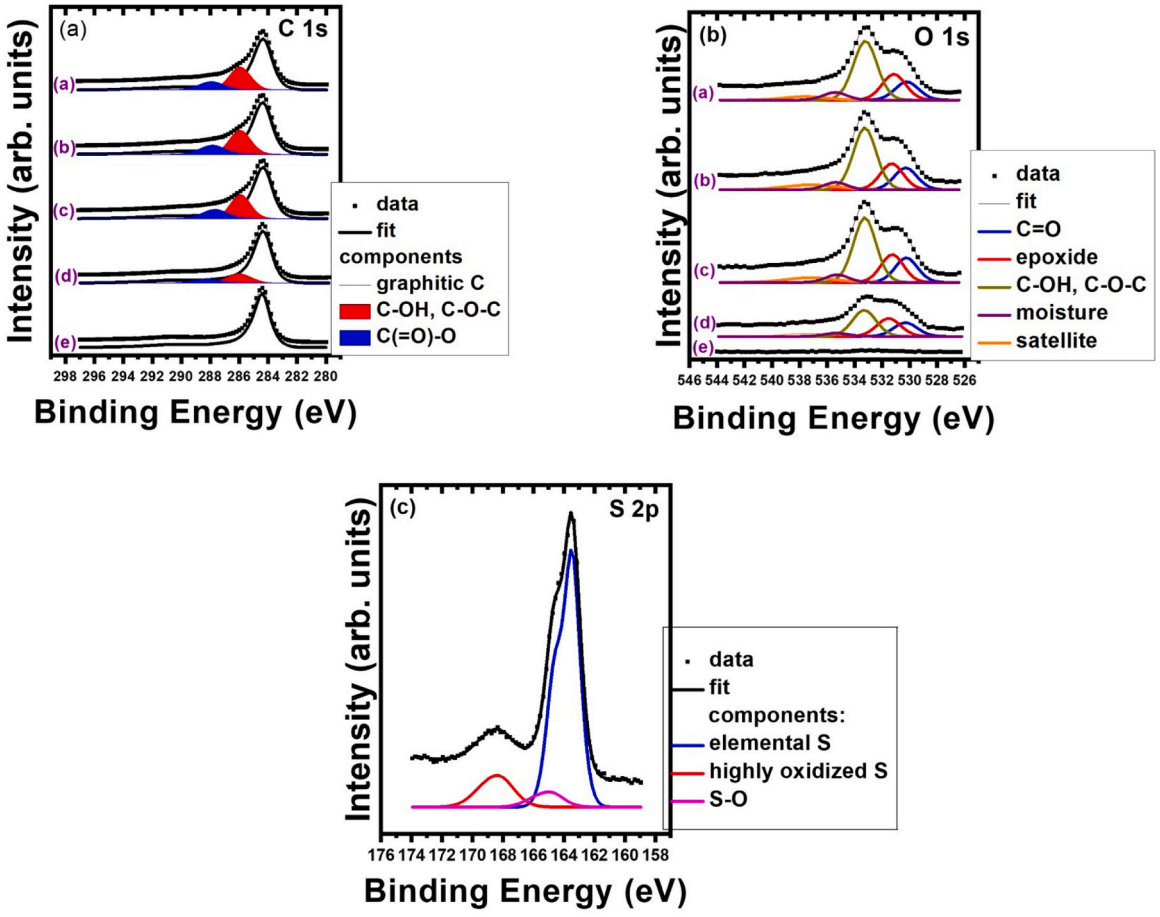

Fig. 6. Panel (a) C 1 s spectra; panel (b) O 1 s spectra of (a) rGO230, (b) rGO350, (c) rGO550, (d) rGO950, and (e) the Super C65 carbon black reference; panel (c) S 2p spectrum of rGO350-S-SCC. The oxygen-bound carbon contributions were multiplied by 3 in panel (a) for better visibility. The intensities of the O 1 s spectra in panel (b) reflect the variation in the amount of oxygen in the samples.

The XPS spectrum of the sulfur-loaded rGO is shown in Fig. 6(c). The main contribution of the S 2p spectrum originated from a $2p_{3/2}$-$2p_{1/2}$ spin-orbit doublet with its leading peak at 163.5 eV, characteristic of elemental sulfur [41]. This confirms the predominance of S-S bonds in the composites. The second wider, well-defined S 2p peak has a binding energy of 168.2 eV, corresponding to oxidized sulfur. However, literature data for many oxidized sulfur forms that involve sulfonyl (SO_2), sulfonate (SO_3), or sulfate (SO_4) functionalities overlap in this binding energy range [41]. Adequate modeling of the spectra required a weak third component arising around 164.8 eV, which can tentatively be assigned to sulfinyl (-SO)- like species [41].

3.1.5. Quantitative analysis by thermogravimetry

Thermogravimetric Analysis (TGA) is performed to quantify the sulfur content in the four rGO-S composite powders. In thermogravimetric analysis, as the composite is heated, sulfur vaporizes and leaves the composite at a specific temperature range, detected as weight loss in the TGA profile. The mass loss corresponding to the vaporization of sulfur helps in determining the sulfur content present in the composites. TGA also provides insights into the thermal stability of the rGO-S composites. By analysing the weight loss at different temperatures, it is possible to determine the temperatures at which the composite materials decompose or react. This information is crucial in understanding the operating temperature range of the battery and ensuring the stability of the cathode material under typical working conditions.

Fig. 7(a-d) shows the thermogram of rGO230-S-SCC, rGO350-S-SCC, rGO550-S-SCC, and rGO950-S-SCC, respectively. The peak at around 60 °C can be attributed to the adsorbed water on the surface. The peaks between 180 and 340°C correspond to the weakly bounded sulfur present on the surfaces and the easily accessible macropores. Sulfur loss ends at around 350–400°C. A peak between 500°C and 550°C corresponds to sulfur infused into mesopores and micropores by the supercritical carbon dioxide treatment. The decomposition of oxygen-containing groups in thermally reduced graphene oxide begins around 500°C, with a continuous mass loss at higher temperatures. Sulfur content was estimated by subtracting the mass loss attributed to water evaporation from the total mass loss at 550°C. Mass loss after 550°C is attributed solely to the decomposition of oxygen-containing groups in the reduced graphene oxide. The estimated sulfur contents (by mass percentage) for rGO230-S-SCC, rGO350-S-SCC, rGO550-S-SCC, and rGO950-S-SCC are 31 %, 51 %, 36 %, and 40 %, respectively. These results establish that sulfur content is directly proportional to the specific surface area and porosity, with rGO350-S-SCC showing the highest sulfur content (51 %), followed by rGO950-S-SCC (40 %), rGO550-S-SCC (36 %), and rGO230-S-SCC (31 %).

3.2. Electrochemical performance of the synthesized rGO/sulfur cathodes

Electrochemical impedance spectroscopy (EIS) measurements were conducted in a two-electrode cell over a frequency range from 100 kHz to 100 mHz using a Bio-Logic (VSP-300) impedance analyzer at a 5 mV sinus amplitude.

The impedance spectra were evaluated using complex nonlinear least squares (CNLS) fitting, with initial values for parameter estimation derived from distribution of relaxation times (DRT) analysis, as described elsewhere [43,44]. The CNLS fitting was performed in Python 3 (Python Software Foundation, Wilmington, DE, USA) using standard scientific packages (NumPy, SciPy, Pandas, Lmfit, and Matplotlib) DRT analysis was performed using pyDRTtools [45].

Fig. 8a shows the complex-plane impedance diagrams of the fabricated coin-type 2032 cells at 100 % state of charge where rGO230-S-SCC, rGO350-S-SCC, rGO550-S-SCC, and rGO950-S-SCC served as the cathode, with lithium metal as the anode, Whatman glass fiber as the separator and 1 M Lithium bis (trifluoromethane sulfonyl) imide (LiTFSi) in 1,2-dimethoxyethane (DME) and 1,3-dioxolane (DOL) (1:1 vol ratio) as the electrolyte.

The overall impedance equation can be written as:

$$Z_{Li-S} = Z_{Ohmic} + Z_{Li} + Z_{RGO-S-SCC} + Z_{diff}$$

Where:

- $Z_{Ohmic} = R_{Ohmic}$ represents the ohmic contribution of the entire cell,

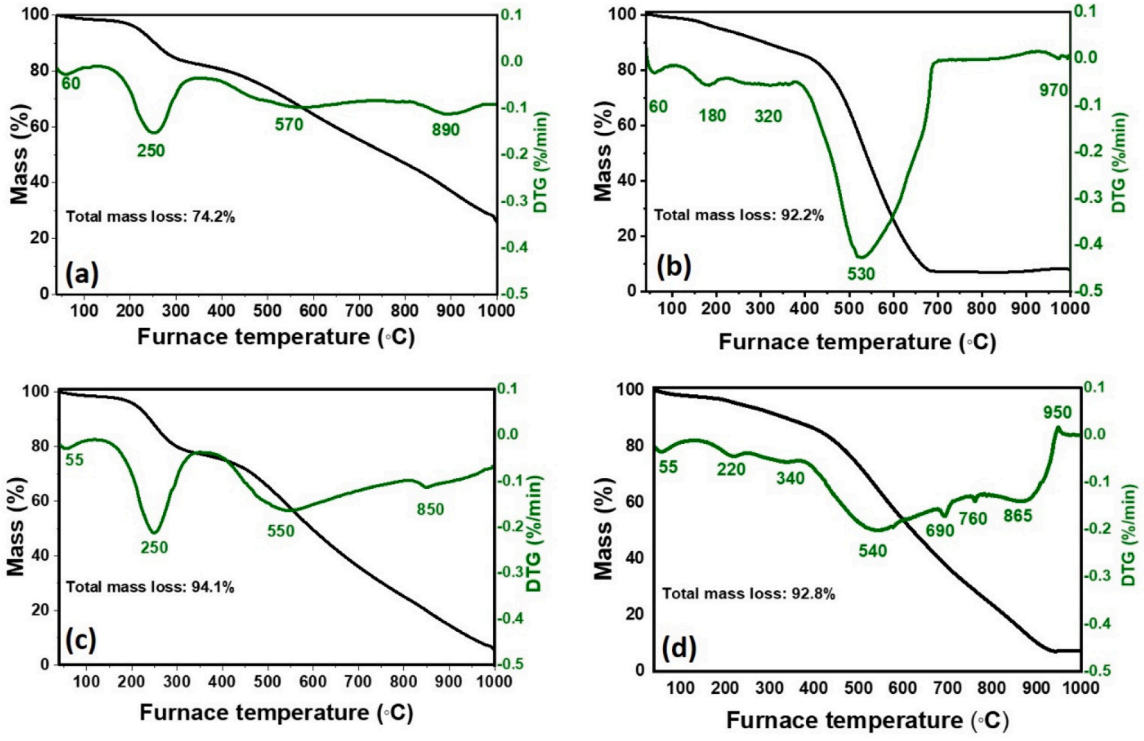

Fig. 7. TG and DTG curves of rGO230-S-SCC, rGO350-S-SCC, rGO550-S-SCC, and rGO950-S-SCC.

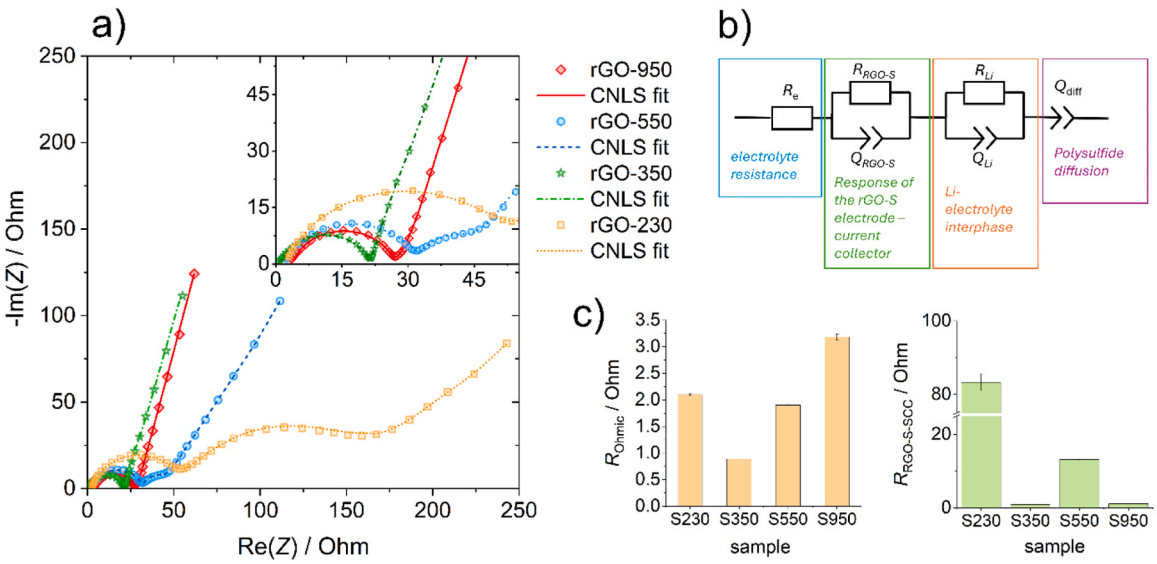

Fig. 8. (a) Complex-plane impedance diagram of rGO230-S-SCC, rGO350-S-SCC, rGO550-S-SCC, and rGO950-S-SCC composite cathodes at 100 % stare-of-charge (the inset shows the high-frequency part of the spectra); (b) equivalent electrical circuit used for fitting the EIS data; (c) R_{Ohmic} and $R_{\text{GO-S-SCC}}$ values of rGO230-S-SCC, rGO350-S-SCC, rGO550-S-SCC, and rGO950-S-SCC with the corresponding standard errors (error bars).

- $Z_{Li} = \frac{R_{Li}}{R_{Li}Q_{Li}(j2\pi f)^{a_{Li}}+1}$ represents the Li-electrolyte interphase contribution,
- $Z_{RGO-S-SCC} = \frac{R_{RGO-S-SCC}}{R_{RGO-S-SCC}Q_{RGO-S-SCC}(j2\pi f)^{a_{RGO-S-SCC}}+1}$ represents the composite electrode contribution,
- Z_{diff} is a constant phase element describing the diffusion of the electrolyte and blocking electronic charge transfer.

Fig. 8b shows the equivalent circuit model used for fitting the EIS data. The model was designed based on the following observations. Changes in the high-frequency region (HF) are mainly due to electrolyte resistance R_{Ohmic} and ohmic contributions from the cell, which are consistent across the four electrode types due to identical electrolyte concentrations, assembly methods, and testing conditions. The near-vertical line observed in the low-frequency (LF) range is attributed to the blocking of electronic charge transfer, preventing the electrochemical reaction. A constant phase element (CPE) was used to model this part of the spectrum [46]. The frequency distribution at the base of the LF straight line can be explained by the diffusion processes through the solid electrolyte interphase (SEI) occurring at the negative electrode. The electrolyte resistance recorded for the as-prepared electrodes is consistent with literature values. The semicircle at 6–9 kHz at the *middle-frequency region* (MF) at the initial state is attributed to the positive electrode and the Li negative electrode responses. Interpreting the semicircle at mid-frequency is a matter of considerable controversy in the literature [46–48]. However, it can be stated with some confidence gained from previous research and based on the distribution of relaxation times (DRT) analysis in our previous work [21] that at least two components contribute to the observed phenomenon. One of them is the sulfur electrode interface, which is due to the blocking (non-conducting) effect of sulfur, and which is a small resistive element. The response is attributed to the polarization of the electrode composite, where the sulfur particles are in contact with the reduced graphene oxide matrix, resulting in contact resistance. In all cases, this contribution is smaller. However, it is observed that in the series of samples, RGO350-S-SCC (0.934 Ohm) and RGO950-S-SCC (1.138 Ohm) have the lowest contact resistance, whereas it is significantly high for RGO550-S-SCC (13.22 Ohm) and RGO230-S-SCC (83.30 Ohm). Fig. 8c shows the calculated resistances for all four samples, and Table 4 shows the CNLS fitting results of the four samples with the corresponding errors of the parameter estimation.

From Fig. 8 and Table 4, in these four sets of rGO-S composite cathodes, the RGO350-S-SCC showed the least impedance followed by RGO950-S-SCC, RGO550-S-SCC and RGO230-S-SCC. Herein, we can see a trend in the total impedance of the cell, which is proportional to the surface area and porosity of the sulfur hosts where rGO350-S-SCC and, subsequently, rGO950-S-SCC show the highest surface area and porosity. This effectively results in better electrolyte penetration and the wetting of the pores, creating close contact between the highly dispersed sulfur nanoparticles and the conductive rGO network, increasing the electronic conductivity.

Following EIS, the galvanostatic charge and discharge cycling of the cells was performed at room temperature in a potential range of 1.5 V to 3.0 V (vs. Li^+ /Li). Fig. 9(a-d) shows the charge-discharge profiles of rGO230-S-SCC, rGO350-S-SCC, rGO550-S-SCC, and rGO950-S-SCC composites at the current rate of 0.2 C.

For a Li-S cell, the cyclo S8 is reduced during discharge, and the ring opens, forming higher-order lithium polysulfides Li_2S_x ($6 < x \leq 8$). With the addition of more lithium, lower-order lithium polysulfides Li_2S_x ($2 < x \leq 6$) are generated as the discharge proceeds. There are two discharge plateaus at 2.3 and 2.1 V, corresponding to the conversions of S_8 to Li_2S_4 and Li_2S_4 to Li_2S, respectively. However, in general, Li-S batteries can exhibit two distinct voltage profiles: one with two plateaus at approximately 2.3 V and 2.1 V, corresponding to a "solid-liquid" dual-phase reaction, and another with a single plateau around 1.8–2 V, indicative of a one-step "solid-phase" reaction typically seen with carbonate-based electrolytes [49–51]. However, some reports have also observed this single plateau with ether-based electrolytes [52–54]. Our earlier research highlighted the exceptional stability of rGO/sulfur composite cathodes with ether-based electrolytes, which achieved a single-step discharge plateau without needing electrolyte additives [21]. The charge-discharge patterns are significantly affected by the carbon host's microstructure and its sulfur and Li-polysulfide adsorption capabilities, as detailed in previous studies. In 2012, Guo and colleagues introduced the idea that "small sulfur molecules" in microporous carbon structures can prevent higher-order polysulfide formation, resulting in a single voltage plateau [52]. This concept evolved to focus on "sulfur chains," which demonstrate high electrochemical activity and produce a one-step plateau [52].

Literature studies have reported the impact of carbon's microstructure and adsorption capacity on electrochemical performance [55]. In this study, from Fig. 9(a-d), it can be observed that the charge-discharge

Table 4
The CNLS fitting results of the four composite cathodes with the corresponding errors of the parameter estimation.

	RGO230-S-SCC		RGO350-S-SCC		RGO550-S-SCC		RGO950-S-SCC	
Parameter	**value**	**standard error**	**value**	**standard error**	**value**	**standard error**	**value**	**standard error**
R_{Ohmic}	2.103	$1.540{\cdot}10^{-2}$	$8.910{\cdot}10^{-1}$	$1.182{\cdot}10^{-1}$	1.902	$2.100{\cdot}10^{-2}$	3.181	$5.560{\cdot}10^{-2}$
R_{Li}	$4.964{\cdot}10^{1}$	$1.520{\cdot}10^{-1}$	$1.962{\cdot}10^{1}$	$4.507{\cdot}10^{-2}$	$2.352{\cdot}10^{1}$	$3.920{\cdot}10^{-2}$	$2.434{\cdot}10^{1}$	$8.030{\cdot}10^{-2}$
Q_{Li}	$1.236{\cdot}10^{-5}$	$7.170{\cdot}10^{-9}$	$2.226{\cdot}10^{-5}$	$1.475{\cdot}10^{-7}$	$2.050{\cdot}10^{-5}$	$1.062{\cdot}10^{-7}$	$2.691{\cdot}10^{-5}$	$6.850{\cdot}10^{-7}$
α_{Li}	$8.024{\cdot}10^{-1}$	$5.694{\cdot}10^{-4}$	$8.498{\cdot}10^{-1}$	$5.050{\cdot}10^{-4}$	$7.815{\cdot}10^{-1}$	$5.050{\cdot}10^{-4}$	$7.810{\cdot}10^{-1}$	$2.649{\cdot}10^{-3}$
$R_{RGO\text{-}S\text{-}SCC}$	$8.330{\cdot}10^{1}$	2.280	$9.340{\cdot}10^{-1}$	$1.84{\cdot}10^{-4}$	$1.322{\cdot}10^{1}$	$9.380{\cdot}10^{-2}$	1.138	$2.682{\cdot}10^{-3}$
$Q_{RGO\text{-}S\text{-}SCC}$	$1.752{\cdot}10^{-3}$	$4.533{\cdot}10^{-7}$	$2.811{\cdot}10^{-5}$	$1.182{\cdot}10^{-6}$	$4.656{\cdot}10^{-3}$	$6.958{\cdot}10^{-5}$	$7.28{\cdot}10^{-2}$	$1.619{\cdot}10^{-3}$
$\alpha_{RGO\text{-}S\text{-}SCC}$	$7.184{\cdot}10^{-1}$	$4.730{\cdot}10^{-4}$	$8.750{\cdot}10^{-1}$	$6.096{\cdot}10^{-4}$	$8.581{\cdot}10^{-1}$	$2.161{\cdot}10^{-3}$	$7.054{\cdot}10^{-1}$	$1.220{\cdot}10^{-5}$
Q_{diff}	$2.140{\cdot}10^{-2}$	$8.080{\cdot}10^{-4}$	$1.700{\cdot}10^{-2}$	$9.405{\cdot}10^{-5}$	$3.565{\cdot}10^{-2}$	$1.080{\cdot}10^{-4}$	$1.519{\cdot}10^{-2}$	$2.906{\cdot}10^{-5}$
α_{diff}	$4.120{\cdot}10^{-1}$	$2.595{\cdot}10^{-3}$	$8.223{\cdot}10^{-1}$	$3.192{\cdot}10^{-3}$	$6.385{\cdot}10^{-1}$	$1.203{\cdot}10^{-3}$	$8.329{\cdot}10^{-1}$	$1.479{\cdot}10^{-3}$

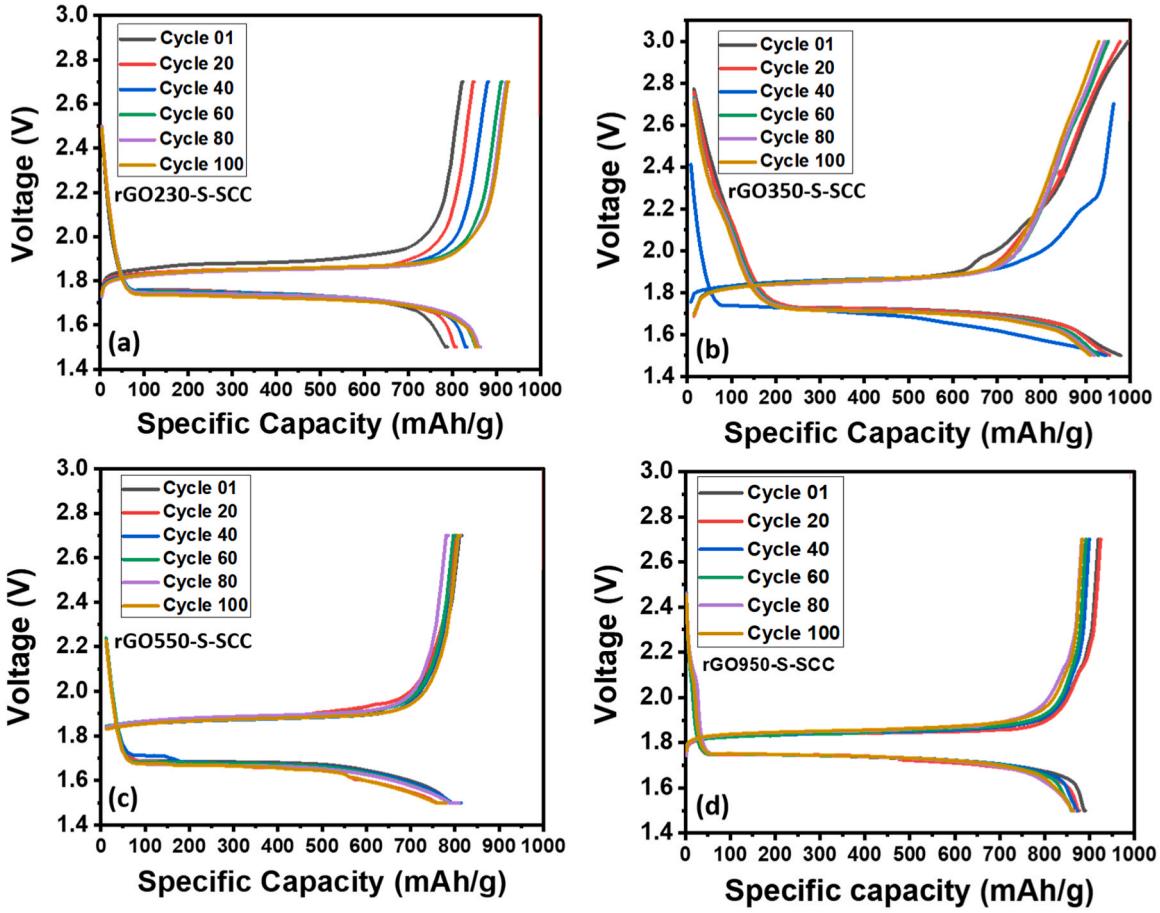

Fig. 9. Charge discharge voltage profiles of (a) rGO230-S-SCC, (b) rGO350-S-SCC, (c) rGO550-S-SCC, and (d) rGO950-S-SCC at 0.2 C rate.

plots do not show the typical two-step voltage plateau. This one-step voltage profile corresponds to the "solid-phase" reaction, unlike the "solid-liquid phase" reaction in conventional Li-S systems. This observation can be validated by the cyclic voltammetry curves as shown in Fig. 10a, where the RGO-S-SCC composite cathodes show only a single reduction peak around 1.9 V vs Li/Li+, corresponding to the reduction of Li_2S_n to lower order polysulfides (Li_2S_2/Li_2S) and diminishing the unfavourable higher order polysulfides. Here, the obtained one-step and long discharge plateau of the four RGO-S-SCC composite cathodes is the distinctive characteristic of the microporous reduced graphene oxide matrix in which the sulfur is embedded. We believe that with the assistance of highly diffusive SC-CO_2, the sulfur molecules penetrated deep into the rGO micropores and that this sulfur confined well within the rGO does not initiate the formation of higher-order polysulfides, eliminating the shuttle effect, resulting in stable electrochemical performances. Moreover, the rGO, with the presence of polar functional groups serves as a strong adsorbing host to the Li-polysulfides and restricts/eliminates the discharge potential hysteresis (which is indicated by higher voltage plateau) formed during the electrochemical reaction. Hence, only a lower voltage plateau is observed for the as-prepared rGO-S-SCC composites.

Out of the investigated samples, the rGO350-S-SCC shows the highest initial specific discharge capacity of 979 $mAhg^{-1}$, followed by rGO950-S-SCC (890 $mAhg^{-1}$), rGO550-S-SCC (808 $mAhg^{-1}$) and rGO230-S-SCC (789 $mAhg^{-1}$). The reason for the trend in electrochemical performance can be explained as follows: the higher surface area of the rGO350 sulfur host, in addition to providing a conductive backbone, can accommodate more sulfur-active material into its internal space. This can be seen in the TG-DTG analysis where rGO350-S-SCC showed the highest sulfur content (51 %) demonstrating the direct correlation between specific surface area, porosity, and the net sulfur content encapsulated inside the rGO backbone. Besides sulfur

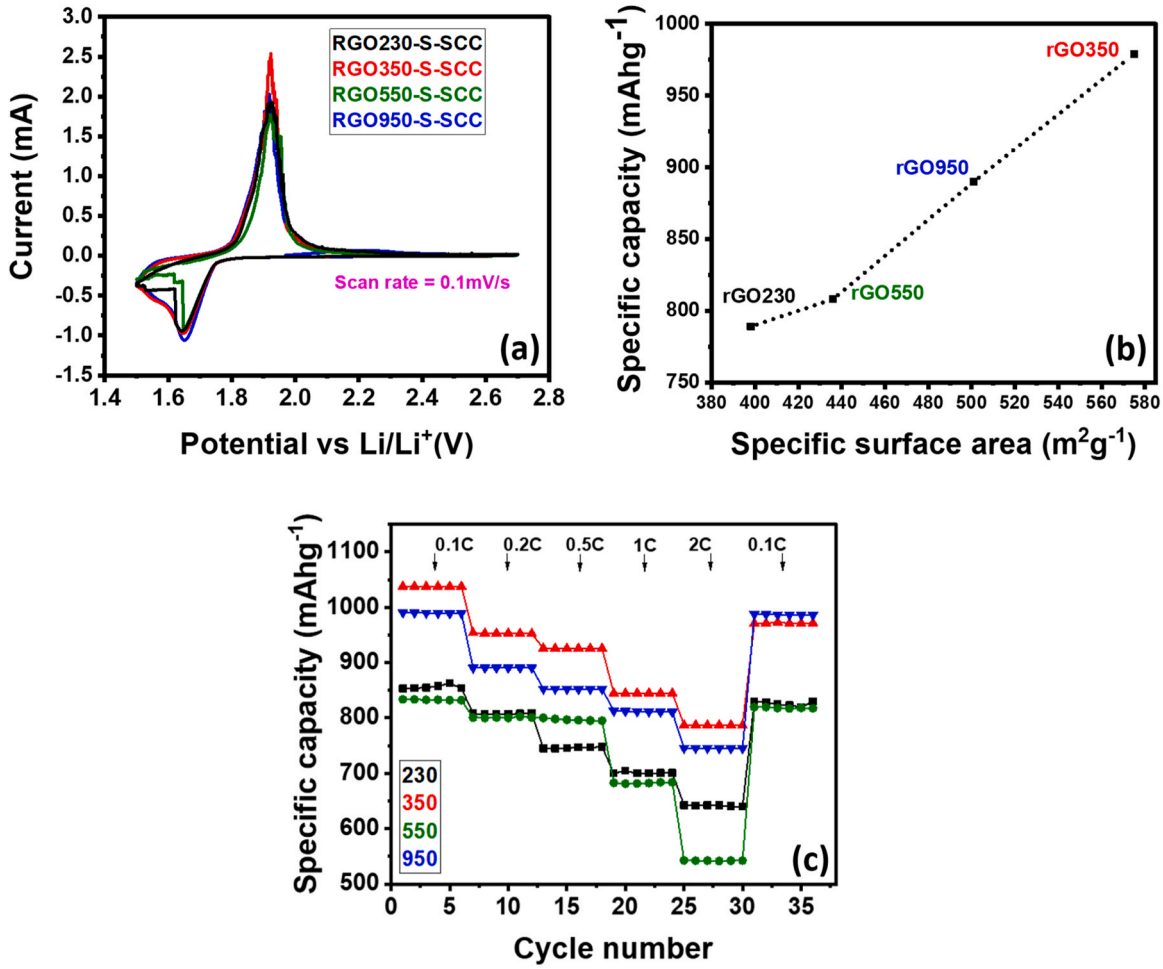

Fig. 10. (a) Cyclic Voltammetry curves for rGO230-S-SCC, rGO350-S-SCC, rGO550-S-SCC, and rGO950-S-SCC at a scan rate of 0.1 mV/s; (b) Relationship between the specific surface area of differently heat-treated rGO and specific discharge capacities of the rGO/sulfur composite cathodes; (c) Rate performance plots for rGO230-S-SCC, rGO350-S-SCC, rGO550-S-SCC, and rGO950-S-SCC.

impregnation, the expanded interlayer space (as evident from the SEM analysis), pores, and increased specific surface area are beneficial to polysulfide trapping and enabling maximum active material utilization during charge-discharge cycling which can significantly enhance the electrochemical performance of the composite cathodes. Furthermore, due to high porosity, the vacant space in the rGO350 architecture can accommodate the volume changes of sulfur particles. This enhanced porosity acts as a buffer, maintaining mechanical stability even during prolonged cycling, which results in long-term cycle stability and high-capacity retention [56,57]. This trend in electrochemical behaviour, driven by the surface properties of rGO and the sulfur content in the composites, is also evident in rGO230-S-SCC, rGO350-S-SCC, and rGO950-S-SCC.

All the composites were prepared with the assistance of the hydrophobic SC-CO_2 solvent, which has low viscosity, high diffusivity, zero surface tension like a gas, and appreciable density and solvation power like a liquid. Its dissolving power can be adjusted by changing pressure and temperature [21]. While the liquid-like density and solvation power of modified SC-CO_2 allows for the dissolution of sulfur, its gas-like diffusivity and viscosity facilitate diffusion and permeation of dissolved sulfur into the depth of micropores and mesopores more rapidly and efficiently. Hence, with the assistance of SC-CO_2, the sulfur particles will be pushed deep into the voids of the rGO matrix, benefiting from encapsulating more active sulfur nanoparticles. The more active sulfur confined within the cathode results in higher discharge capacity and long-term cycling stability. This is evident in the long-term cycling tests where the rGO350-S-SCC cell shows a capacity retention of 96.52 % even after 100 charge-discharge cycles. The capacity retention of other composites, rGO550-S-SCC and rGO950-S-SCC is 96.28 % and 96.40 %, respectively. On the other hand, rGO230-S-SCC shows a continuous increase in the specific discharge capacity. This trend of increasing capacity and good cycle stability indicates the strong affinity of discharge products on the highly functionalized rGO. The initial discharge capacity trend was reported before [30,58–62]. For example, a similar increase in capacity was also noted for the sulfur and hollow carbon nanofiber nanocomposite that was altered with amphiphilic polymers [63].

From the observations in this study, a linear relationship between the accessible surface area and specific discharge capacity is established, as shown in Fig. 10b. The results show that the cathode capacity can be directly associated with the structural and chemical changes of the carbonaceous materials, such as the transition from the amorphous over the turbostratic phase to the graphitic phase and the removal of foreign atoms like hydrogen. This shows that the temperature plays a significant role in the surface engineering of carbon materials, influencing the electrochemical performance of the as-prepared carbon/sulfur composite cathodes.

The cells were subjected to charge-discharge cycles and various current densities to comprehend their performance in extreme conditions. Fig. 10c shows the rate performance plots for all four composite cathodes- rGO230-S-SCC, rGO350-S-SCC, rGO550-S-SCC, and rGO950-S-SCC. The rate capability tests were performed at various current

rates ranging from 0.1 C to 2 C. As seen in Fig. 10c, the initial specific discharge capacity of rGO350-S-SCC is consistently higher at low as well as high current rates (except for a trivial difference when the cell is switched back to 0.1 C rate) compared to other composite cathodes. For all the composites, moving from a lower current rate (0.1 C) to the highest current rate (2 C), the discharge capacity degrades, and then this capacity is again recovered to 99 %- 99.5 % of its initial state when the cell is abruptly switched back to 0.1 C rate indicating the excellent robustness and stability of the as-prepared nanocomposites.

From the overall electrochemical performance evaluation, rGO350-S-SCC shows the highest specific discharge capacity, and highest capacity retention, followed by rGO950-S-SCC, rGO550-S-SCC, and rGO230-S-SCC. This indicates that strategic control/optimization of the variables morphology, surface area, and porosity has a distinct role and importance in enabling maximum accessible active sulfur loading, resulting in enhanced and long-term cycling stability of nanocomposite cathodes.

To evaluate the electrochemical performance of the synthesized rGO/sulfur composite cathodes, a comparative analysis was conducted with carbon-sulfur composites reported in previous studies. Table 5 provides a comparison of the performance metrics of the rGO/sulfur composites developed in this work with other composites synthesized through different routes.

A recent study has compared the electrochemical performances of Li-S cathodes prepared by different synthesis routes, stating the importance of composite preparation on the effective electrochemical behaviour of the cell [32]. The work compared the four synthesis routes: melt diffusion, ball milling, dissolution crystallization, and chemical deposition. However, compared to these reports, the rGO/S composite cathodes developed in this work showed much enhanced electrochemical performances, highlighting the efficiency of the SC-CO_2-assisted synthesis route than the conventional cathode synthesis strategies. As we have prepared the rGO/sulfur composites using the supercritical CO_2 technology, the comparison shown in Table 5 is done only with the composites synthesized in the same route Notably, even at a higher current rate of 0.2 C, the rGO/sulfur composite cathodes synthesised in this study demonstrate superior electrochemical performance, especially in terms of long-term cycling stability, when compared to composites such as activated-carbon-sulfur, MWCNT-sulfur, C/CeO_2/S, and MCMB-sulfur composites cycled at a 0.1 C rate.

This reinforces that the careful selection of a highly conductive carbon framework (rGO) and optimization of surface chemistry through thermal treatment, coupled with an environmentally friendly synthesis process (SC-CO_2), plays a synergistic role in achieving high-performance carbon-sulfur composite cathodes for Li-S batteries.

4. Conclusions

In this work, four differently reduced rGOs are produced by thermal treatment, and the influence of reduction temperature on the morphology, chemical structure, surface chemistry, and, subsequently, the overall electrochemical performance of the as-prepared rGO/sulfur nanocomposite cathodes are investigated. The results show that the thermally reduced GO possesses an interconnected network of micro, meso-, and macro porosity and a wide range of specific surface areas depending on the reduction conditions. SEM images reveal that all four rGOs have wrinkled and folded layered morphology, with rGO350-S-SCC showing a distinctively transparent, paper-like, and more open porous structure. The homogenous distribution of sulfur in the rGO framework is confirmed by TEM coupled with HAADF-EDS analysis. The SAED analysis revealed an increased interlayer distance upon adding sulfur nanoparticles to the rGO, showing the successful encapsulation of sulfur into the rGO backbone. This layered and open porous structure facilitates better the deep penetration of electrolyte ions and more effective dispersion of active sulfur particles into the rGO structure, boosting electronic conductivity and contributing to improved electrochemical performance of the composite cathodes. It is worth noting that the voltage profile of the four composite cathodes showed a single discharge plateau owing to the one-step “solid-phase” reaction where the transition from S8 to S_4^{2-} is eliminated, resulting in the elimination of highly soluble higher-order polysulfides, which in turn helped attain highly stable, longer life and efficient composite cathodes. Out of the investigated samples, the rGO350-S-SCC shows the highest initial specific discharge capacity of 979 $mAhg^{-1}$, followed by rGO950-S-SCC (890 $mAhg^{-1}$), rGO550-S-SCC (808 $mAhg^{-1}$) and rGO230-S-SCC (789 $mAhg^{-1}$). Among the various reduced graphene oxide (rGO) samples studied, the rGO350 demonstrated the highest surface area and porosity as analyzed by Brunauer–Emmett–Teller (BET) measurements. This increased surface area and porosity are crucial because they enable the host material to accommodate more active sulfur (as evident from TG-DTG analysis), enabling greater utilization of active materials, resulting in enhanced cycle life of the cell. The high porosity of rGO350 plays a dual role. First, it provides ample vacant space within the architecture to accommodate the volumetric changes of sulfur particles that occur during cycling. This prevents the degradation of the mechanical structure of the cathode, thus contributing to its stability over prolonged cycles. Second, the increased porosity enhances the physical immobilization of the sulfur particles, reducing their tendency to form unfavourable higher order polysulfides, mitigating the shuttle effect and thereby enhancing the electrochemical performance. This work establishes a linear correlation between the specific area, porosity, active sulfur content and electrochemical performance of the rGO/sulfur composite cathodes. The observation that rGO350 shows the best results compared to the rGO prepared at higher temperatures opens a promising possibility to develop the most suitable sulfur host with low-temperature requirements. In addition to the surface chemistry, changes in the chemical structure of rGO in the selected reduction change were analysed. Results from XRD and Raman analysis show that no significant

Table 5
A comparative analysis of the electrochemical performance of the rGO/sulfur-composites synthesized in this work with earlier reported results.

Type of carbon-sulfur composite	Current rate (C)	Initial discharge capacity ($mAhg^{-1}$)	Cycle number (N)	Discharge capacity after ‘N’ cycles ($mAhg^{-1}$)	Capacity retention after ‘N’ cycles (%)
rGO230-S-SCC	0.2	789	100	859	Capacity enhancement after initial cycles
rGO350-S-SCC	0.2	979	100	945	96.52
rGO550-S-SCC	0.2	808	100	778	96.28
rGO950-S-SCC	0.2	890	100	858	96.40
Activated carbon-sulfur [64]	0.1	905	100	817	90.5
MWCNT-sulfur [64]	0.1	861	100	441	51.2
MCMB-sulfur [64]	0.1	807	100	715	88.6
C/CeO_2/S [65]	0.1	1538	100	929	60.40
Activated carbon-sulfur [66]	0.5	701	150	420	60
Ni(OH)@Porous yeast carbon-sulfur [67]	0.2	1173	200	602	51.3

change in chemical structure has taken place between 230 degrees to 950 degrees. According to XPS results, the C/O ratio does not show any monotonous trend, indicating no direct correlation between the temperature of GO reduction and the C/O ratio.

In this work, one of the noteworthy features of the rGO synthesis is that no external functionalization agents and toxic reducing agents/co-solvents are added. Additionally, unlike conventional cathode synthesis routes, the rGO/sulfur composite cathodes are prepared at room temperature, eliminating the need for high energy consumption. These results are clear indicators of understanding the importance of the balance between the complementary approaches: (1) the choice of rGO as sulfur host, (2) fine-tuning of the morphology, porosity, and surface chemistry of the sulfur host by non-toxic thermal treatment, and (3) the nanocomposite synthesis strategy (supercritical CO_2 technology) in enhancing the overall electrochemical performance of the Li-S nanocomposite cathodes.

5. Challenges and the future Perspectives of utilizing SC-CO_2 technology in composite cathode preparation

Despite its numerous benefits, SC-CO_2 technology is still in its pilot stages. One major challenge is the high pressure required to maintain CO_2 in its supercritical state, necessitating specialized and costly equipment. Developing durable, cost-effective materials for high-pressure vessels and components is essential. Another concern is maintaining the precise temperature range required for SC-CO_2 (above 31.1°C), where achieving uniform temperature distribution can be difficult. However, developing advanced control and monitoring systems could ensure accurate temperature management throughout the process. Additionally, more in-depth research and optimization are needed for the control parameters and reaction mechanisms of SC-CO_2-assisted synthesis. Specific parameters such as temperature, pressure, and reaction time need further optimization. Most studies focus on temperatures around 32°C, pressures between 7 MPa and 10 MPa, and reaction times of 3–12 hours. However, extensive studies on the effects of these parameters on:

1. The solubility of sulfur
2. Microstructural changes in composite materials
3. Physical and chemical interactions between CO_2 and the active material under different conditions
4. Surface chemistry of composites synthesized under various conditions

The overall electrochemical performance of composite cathodes highly depends on these factors. Therefore, various trial-and-error experiments or a design of experiment (DOE) approach are needed to understand the relationship between pressure, temperature, time, and CO_2 flow rate with the solubility and diffusivity of sulfur under different conditions. Another aspect is that the scaling up SC-CO_2-assisted synthesis of nanocomposites requires a highly skilled workforce and strict safety protocols due to the high-pressure reactor systems used. Considering the financial aspect, conducting a thorough cost-benefit analysis to identify scenarios where the benefits of using SC-CO_2 outweigh the costs is crucial. There is also a gap in teaching and awareness regarding these advanced synthesis technologies, as textbooks often overlook unusual reaction media. Increased awareness within the research community is essential to support these innovative methods for a more environmentally friendly future.

In conclusion, while there are challenges, they can be overcome with innovative research, innovative technology, and strategic planning. SC-CO_2-assisted synthesis holds immense potential for the rational design and controllable synthesis of carbon/sulfur composite cathodes for Li–S batteries, offering a sustainable and efficient approach with detailed research.

CRediT authorship contribution statement

Katalin Balázsi: Methodology, Investigation. **Zoltán Pászti:** Methodology, Investigation. **Levente Illés:** Methodology, Investigation. **Zsolt Czigány:** Methodology, Investigation. **Márton Szabados:** Methodology. **Peter B. Nagy:** Methodology. **Dóra Zalka:** Methodology. **Lakshmi Shiva Shankar:** Writing – original draft, Methodology, Investigation, Data curation. **Robert Kun:** Writing – review & editing, Supervision, Funding acquisition, Conceptualization. **Krisztina László:** Methodology, Investigation. **Samantha K. Samaniego Andrade:** Methodology, Investigation.

Declaration of Competing Interest

The authors declare that they have no known competing financial interests or personal relationships that could have appeared to influence the work reported in this paper.

Data availability

Data will be made available on request.

Acknowledgements

The authors thank Edit Szekely and Marton Korosi, Department of Physical Chemistry and Materials Science, Faculty of Chemical Technology and Biotechnology, Budapest University of Technology and Economics, for the experimental support.

The authors thank Tamas Szabo, Department of Physical Chemistry and Materials Science, University of Szeged, for experimental support.

The authors thank the financial support from Project No. RRF-2.3.1-21-2022-00009, titled National Laboratory for Renewable Energy that has been implemented with the support provided by the Recovery and Resilience Facility of the European Union within the framework of Programme Széchenyi Plan Plus. This research was supported by the grant no. VEKOP-2.3.3-15-2016-00002 and VEKOP-2.3.2-16-2016-00011 of the European Structural and Investment Funds.

References

[1] M. Wang, Z. Bai, T. Yang, C. Nie, X. Xu, Y. Wang, J. Yang, S. Dou, N. Wang, Advances in high sulfur loading cathodes for practical lithium-sulfur batteries, Adv. Energy Mater. 12 (2022) 2201585, https://doi.org/10.1002/aenm.202201585.

[2] H. Ye, Y. Li, Room-temperature metal–sulfur batteries: what can we learn from lithium–sulfur? InfoMat 4 (2022) e12291 https://doi.org/10.1002/inf2.12291.

[3] J. Sun, T. Wang, Y. Gao, Z. Pan, R. Hu, J. Wang, Will lithium-sulfur batteries be the next beyond-lithium ion batteries and even much better? InfoMat 4 (2022) e12359 https://doi.org/10.1002/inf2.12359.

[4] F. Zhao, J. Xue, W. Shao, H. Yu, W. Huang, J. Xiao, Toward high-sulfur-content, high-performance lithium-sulfur batteries: review of materials and technologies, J. Energy Chem. 80 (2023) 625–657, https://doi.org/10.1016/j.jechem.2023.02.009.

[5] W. Yao, K. Liao, T. Lai, H. Sul, A. Manthiram, Rechargeable metal-sulfur batteries: key materials to mechanisms, Chem. Rev. 124 (2024) 4935–5118, https://doi.org/10.1021/acs.chemrev.3c00919.

[6] S. Kaskel, J.Q. Huang, H. Sakaebe, Lithium-sulfur batteries: current achievements and further development, Batter. Supercaps 5 (2022) e202200467, https://doi.org/10.1002/batt.202200467.

[7] C. He, Z.F. Qi, W.X. Zhang, Design of transition metal carbonitrides (MCNs) as promising anchoring and high catalytic performance materials for lithium-sulfur batteries, J. Alloy. Compd. 934 (2023) 167786, https://doi.org/10.1016/J.JALLCOM.2022.167786.

[8] Y. Shi, K. Zhang, H. Wang, T. Wan, L. Wu, G. Liu, Reduced graphene oxide wrapped ZnCo layered double hydroxides microsphere as efficient sulfur host in lithium-sulfur batteries, J. Alloy. Compd. 968 (2023) 172059, https://doi.org/10.1016/J.JALLCOM.2023.172059.

[9] Y. Zhang, J. Guo, J. Ren, Z. Chen, M. Zhang, Z. Li, Selenium defects of 2D VSe2/CNTs composite as an efficient sulfur host for high-performance Li-S batteries, J. Alloy. Compd. 951 (2023) 169820, https://doi.org/10.1016/j.jallcom.2023.169820.

[10] W. Feng, J. Chen, Y. Niu, W. Zhao, L. Zhang, CeO2 composite metal organic framework is used to construct high-performance lithium-sulfur batteries, J. Alloy. Compd. 906 (2022) 164341, https://doi.org/10.1016/j.jallcom.2022.164341.

[11] H. Hu, H. Chen, W. Wang, S. Li, Y. Zhang, J. Liu, Y. Zheng, Synthesis of nickel@N-doped carbon nanotube foams for high sulfur-loading lithium-sulfur battery, J. Alloy. Compd. 922 (2022) 166263, https://doi.org/10.1016/j.jallcom.2022.166263.
[12] Y. Guo, Q. Niu, F. Pei, Q. Wang, Y. Zhang, L. Du, Y. Zhang, Y. Zhang, Y. Zhang, L. Fan, Q. Zhang, L. Yuan, Y. Huang, Interface engineering toward stable lithium-sulfur batteries, Energy Environ. Sci. 17 (2024) 1330–1367, https://doi.org/10.1039/d3ee04183b.
[13] S. Tiwari, V. Yadav, A.K. Poonia, D. Pal, Exploring advances in sulfur composite cathodes for lithium-sulfur batteries: a comprehensive review, J. Energy Storage 94 (2024) 112347, https://doi.org/10.1016/J.EST.2024.112347.
[14] J.P. Grace, M. Bhar, S. Ghosh, S.K. Martha, 3D Electrode architecture of high surface area carbon-sulfur composite as high energy density cathode for lithium-sulfur battery, J. Alloy. Compd. 969 (2023), https://doi.org/10.1016/j.jallcom.2023.172341.
[15] M.L. Para, C.A. Calderón, S. Drvarič Talian, F. Fischer, G.L. Luque, D.E. Barraco, E. P.M. Leiva, R. Dominko, Extending the conversion rate of sulfur infiltrated into microporous carbon in carbonate electrolytes, Batter. Supercaps 5 (2022) e202100374, https://doi.org/10.1002/batt.202100374.
[16] L. Li, Z. Ma, Y. Li, Accurate determination of optimal sulfur content in mesoporous carbon hosts for high-capacity stable lithium-sulfur batteries, Carbon 197 (2022) 200–208, https://doi.org/10.1016/j.carbon.2022.06.036.
[17] Y. Xiang, L. Lu, A.G.P. Kottapalli, Y. Pei, Status and perspectives of hierarchical porous carbon materials in terms of high-performance lithium–sulfur batteries, Carbon Energy 4 (2022) 346–398, https://doi.org/10.1002/cey2.185.
[18] A. Manthiram, Y. Fu, S.H. Chung, C. Zu, Y.S. Su, Rechargeable lithium-sulfur batteries, Chem. Rev. 114 (2014) 11751–11787, https://doi.org/10.1021/cr500062v.
[19] Q. Pang, X. Liang, C.Y. Kwok, L.F. Nazar, Advances in lithium-sulfur batteries based on multifunctional cathodes and electrolytes, Nat. Energy 1 (2016) 16132, https://doi.org/10.1038/nenergy.2016.132.
[20] J. Sun, J.Y. Hwang, P. Jankowski, L. Xiao, J.S. Sanchez, Z. Xia, S. Lee, A.V. Talyzin, A. Matic, V. Palermo, Y.K. Sun, M. Agostini, Critical role of functional groups containing N, S, and O on graphene surface for stable and fast charging Li-S batteries, Small 17 (2021) 2007242, https://doi.org/10.1002/smll.202007242.
[21] L.S. Shankar, D. Zalka, T. Szabó, E. Székely, M. Kőrösi, Z. Pászti, K. Balázsi, L. Illés, Z. Czigány, R. Kun, Supercritical carbon dioxide assisted synthesis of ultra-stable sulfur/carbon composite cathodes for Li– S batteries, Mater. Today Chem. 26 (2022) 101240, https://doi.org/10.1016/j.mtchem.2022.101240.
[22] M.M. Amaral, S. Bin Mujib, E.A. Santos, J. Ribeiro, H. Zanin, G. Singh, A sulfur host based on silicon oxycarbide for advanced lithium-sulfur batteries, J. Energy Storage 72 (2023) 108388, https://doi.org/10.1016/j.est.2023.108388.
[23] F. Wu, J.T. Lee, E. Zhao, B. Zhang, G. Yushin, Graphene-Li2S-carbon nanocomposite for lithium-sulfur batteries, ACS Nano 10 (2016) 1333–1340, https://doi.org/10.1021/acsnano.5b06716.
[24] P.R. Adhikari, E. Lee, L. Smith, J. Kim, S. Shi, W. Choi, Effect of morphological variation in three-dimensional multiwall carbon nanotubes as the host cathode material for high-performance rechargeable lithium-sulfur batteries, RSC Adv. 13 (2023) 9402–9412, https://doi.org/10.1039/d3ra00502j.
[25] G. Yang, R. Tao, C.J. Jafta, C. Shen, S. Zhao, L. He, I. Belharouak, J. Nanda, Investigating multiscale spatial distribution of sulfur in a CNT scaffold and its impact on Li-S cell performance, J. Phys. Chem. C 125 (2021) 13146–13157, https://doi.org/10.1021/acs.jpcc.1c02288.
[26] F.F. Zhang, X.B. Zhang, Y.H. Dong, L.M. Wang, Facile and effective synthesis of reduced graphene oxide encapsulated sulfur via oil/water system for high performance lithium sulfur cells, J. Mater. Chem. 22 (2012) 11452–11454, https://doi.org/10.1039/c2jm16543k.
[27] G. Li, J. Sun, W. Hou, S. Jiang, Y. Huang, J. Geng, Three-dimensional porous carbon composites containing high sulfur nanoparticle content for high-performance lithium-sulfur batteries, Nat. Commun. 7 (2016) 10607, https://doi.org/10.1038/ncomms10601.
[28] C. Hernández-Rentero, R. Córdoba, N. Moreno, A. Caballero, J. Morales, M. Olivares-Marín, V. Gómez-Serrano, Low-cost disordered carbons for Li/S batteries: A high-performance carbon with dual porosity derived from cherry pits, Nano Res. 11 (2018) 89–100, https://doi.org/10.1007/s12274-017-1608-1.
[29] Y.S. Su, A. Manthiram, A facile in situ sulfur deposition route to obtain carbon-wrapped sulfur composite cathodes for lithium-sulfur batteries, Electrochim. Acta 77 (2012) 272–278, https://doi.org/10.1016/j.electacta.2012.06.002.
[30] H. Wang, Y. Yang, Y. Liang, J.T. Robinson, Y. Li, A. Jackson, Y. Cui, H. Dai, Graphene-wrapped sulfur particles as a rechargeable lithium-sulfur battery cathode material with high capacity and cycling stability, Nano Lett. 11 (2011) 2644–2647, https://doi.org/10.1021/nl200658a.
[31] S. Zhao, X. Zhang, C. Ma, Y. Liu, W. Zhang, Y. Zhao, Fabrication of tantalum carbide cathode by ball milling processes for advanced lithium–sulfur batteries, J. Mater. Sci. 58 (2023) 7407–7417, https://doi.org/10.1007/s10853-023-08331-8.
[32] Á. Bonilla, A. Benítez, J.L. Gómez-Cámer, Á. Caballero, Impact of composite preparation method on the electrochemical performance of lithium–sulfur batteries, J. Alloy. Compd. 968 (2023) 171810, https://doi.org/10.1016/j.jallcom.2023.171810.
[33] P.B. Arthi G, L. BD, A simple approach to stepwise synthesis of graphene oxide nanomaterial, J. Nanomed. Nanotechnol. 06 (2015) 1000253, https://doi.org/10.4172/2157-7439.1000253.
[34] M. Thommes, K. Kaneko, A.V. Neimark, J.P. Olivier, F. Rodriguez-Reinoso, J. Rouquerol, K.S.W. Sing, Physisorption of gases, with special reference to the evaluation of surface area and pore size distribution (IUPAC Technical Report), Pure Appl. Chem. 87 (2015) 1051–1069, https://doi.org/10.1515/pac-2014-1117.
[35] R.P. Rocha, M.F.R. Pereira, J.L. Figueiredo, Characterisation of the surface chemistry of carbon materials by temperature-programmed desorption: an assessment, Catal. Today 418 (2023) 114136, https://doi.org/10.1016/j.cattod.2023.114136.
[36] R. Siburian, H. Sihotang, S. Lumban Raja, M. Supeno, C. Simanjuntak, New route to synthesize of graphene nano sheets, Orient. J. Chem. 34 (2018) 182–187, https://doi.org/10.13005/ojc/340120.
[37] H.H. Huang, K.K.H. De Silva, G.R.A. Kumara, M. Yoshimura, Structural evolution of hydrothermally derived reduced graphene oxide, Sci. Rep. 8 (2018) 6849, https://doi.org/10.1038/s41598-018-25194-1.
[38] S.J. Qiao, X.N. Xu, Y. Qiu, H.C. Xiao, Y.F. Zhu, Simultaneous reduction and functionalization of graphene oxide by 4-hydrazinobenzenesulfonic acid for polymer nanocomposites, Nanomaterials 6 (2016) 29, https://doi.org/10.3390/nano6020029.
[39] J. Wang, Y. Liu, M. Cheng, H. Zhao, J. Wang, Z. Zhao, X. Duan, C. Wang, J. Wang, Hierarchical porous carbon-graphene-based Lithium–Sulfur batteries, Electrochim. Acta 318 (2019) 161–168, https://doi.org/10.1016/j.electacta.2019.05.090.
[40] Y. Yamada, H. Yasuda, K. Murota, M. Nakamura, T. Sodesawa, S. Sato, Analysis of heat-treated graphite oxide by X-ray photoelectron spectroscopy, J. Mater. Sci. 48 (2013) 8171–8198, https://doi.org/10.1007/s10853-013-7630-0.
[41] NIST X-ray Photoelectron Spectroscopy Database, NIST Standard Reference Database Number 20, National Institute of Standards and Technology, Gaithersburg MD, 20899 (2000), https://dx.doi.org/10.18434/T4T88K.
[42] L. Stobinski, B. Lesiak, J. Zemek, P. Jiricek, Time dependent thermal treatment of oxidized MWCNTs studied by the electron and mass spectroscopy methods, Appl. Surf. Sci. 258 (2012) 7912–7917, https://doi.org/10.1016/J.APSUSC.2012.04.127.
[43] J.P. Schmidt, T. Chrobak, M. Ender, J. Illig, D. Klotz, E. Ivers-Tiffée, Studies on LiFePO4 as cathode material using impedance spectroscopy, J. Power Sources 196 (2011) 5342–5348, https://doi.org/10.1016/j.jpowsour.2010.09.121.
[44] J.P. Schmidt, P. Berg, M. Schönleber, A. Weber, E. Ivers-Tiffée, The distribution of relaxation times as basis for generalized time-domain models for Li-ion batteries, J. Power Sources 221 (2013) 70–77, https://doi.org/10.1016/j.jpowsour.2012.07.100.
[45] T.H. Wan, M. Saccoccio, C. Chen, F. Ciucci, Influence of the discretization methods on the distribution of relaxation times deconvolution: implementing radial basis functions with DRTtools, Electrochim. Acta 184 (2015) 483–499, https://doi.org/10.1016/j.electacta.2015.09.097.
[46] S. Waluś, C. Barchasz, R. Bouchet, F. Alloin, Electrochemical impedance spectroscopy study of lithium–sulfur batteries: useful technique to reveal the Li/S electrochemical mechanism, Electrochim. Acta 359 (2020) 136944, https://doi.org/10.1016/j.electacta.2020.136944.
[47] M. Hagen, G. Feisthammel, P. Fanz, H.T. Grossmann, S. Dörfler, J. Tübke, M. J. Hoffmann, D. Börner, M. Joos, H. Althues, S. Kaskel, Sulfur cathodes with carbon current collector for Li-S cells, J. Electrochem. Soc. 160 (2013) A996–A1002, https://doi.org/10.1149/2.149306jes.
[48] Z. Deng, Z. Zhang, Y. Lai, J. Liu, J. Li, Y. Liu, Electrochemical impedance spectroscopy study of a lithium/sulfur battery: modeling and analysis of capacity fading, J. Electrochem. Soc. 160 (2013) A553–A558, https://doi.org/10.1149/2.026304jes.
[49] X. Yang, X. Li, K. Adair, H. Zhang, X. Sun, Structural design of lithium–sulfur batteries: from fundamental research to practical application, Electrochem. Energy Rev. 1 (2018) 239–293, https://doi.org/10.1007/s41918-018-0010-3.
[50] R. Pai, A. Singh, M.H. Tang, V. Kalra, Stabilization of gamma sulfur at room temperature to enable the use of carbonate electrolyte in Li-S batteries, Commun. Chem. 5 (2022) 17, https://doi.org/10.1038/s42004-022-00626-2.
[51] S.S. Zhang, Liquid electrolyte lithium/sulfur battery: Fundamental chemistry, problems, and solutions, J. Power Sources 231 (2013) 153–162, https://doi.org/10.1016/j.jpowsour.2012.12.102.
[52] C.P. Yang, Y.X. Yin, Y.G. Guo, L.J. Wan, Electrochemical (De)lithiation of 1D sulfur chains in Li-S batteries: a model system study, J. Am. Chem. Soc. 137 (2015) 2215–2218, https://doi.org/10.1021/ja513009v.
[53] S. Xin, L. Gu, N.H. Zhao, Y.X. Yin, L.J. Zhou, Y.G. Guo, L.J. Wan, Smaller sulfur molecules promise better lithium'sulfur batteries, J. Am. Chem. Soc. 134 (2012) 18510–18513, https://doi.org/10.1021/ja308170k.
[54] X. Huang, Z. Wang, R. Knibbe, B. Luo, S.A. Ahad, D. Sun, L. Wang, Cyclic voltammetry in lithium–sulfur batteries—challenges and opportunities, Energy Technol. 7 (2019) 1801001, https://doi.org/10.1002/ente.201801001.
[55] B. Zhang, X. Qin, G.R. Li, X.P. Gao, Enhancement of long stability of sulfur cathode by encapsulating sulfur into micropores of carbon spheres, Energy Environ. Sci. 3 (2010) 1531–1537, https://doi.org/10.1039/c002639e.
[56] D.A. Dornbusch, R. Hilton, M.J. Gordon, G.J. Suppes, Effects of carbon surface area on performance of lithium sulfur battery cathodes, J. Ind. Eng. Chem. 19 (2013) 1968–1972, https://doi.org/10.1016/j.jiec.2013.03.005.
[57] J. Zhang, M. Huang, B. Xi, K. Mi, A. Yuan, S. Xiong, Systematic study of effect on enhancing specific capacity and electrochemical behaviors of lithium–sulfur batteries, Adv. Energy Mater. 8 (2018) 1701330, https://doi.org/10.1002/aenm.201701330.
[58] P.J.H. Kim, K. Kim, V.G. Pol, Towards highly stable lithium sulfur batteries: surface functionalization of carbon nanotube scaffold, Carbon 131 (2018) 175–183, https://doi.org/10.1016/j.carbon.2018.01.100.
[59] Z. Wang, Y. Dong, H. Li, Z. Zhao, H. Bin Wu, C. Hao, S. Liu, J. Qiu, X.W.D. Lou, Enhancing lithium-sulphur battery performance by strongly binding the discharge

products on amino-functionalized reduced graphene oxide, Nat. Commun. 5 (2014) 5002, https://doi.org/10.1038/ncomms6002.
[60] L. Ji, M. Rao, H. Zheng, L. Zhang, Y. Li, W. Duan, J. Guo, E.J. Cairns, Y. Zhang, Graphene oxide as a sulfur immobilizer in high performance lithium/sulfur cells, J. Am. Chem. Soc. 133 (2011) 18522–18525, https://doi.org/10.1021/ja206955k.
[61] J.W. Kim, J.D. Ocon, D.W. Park, J. Lee, Functionalized graphene-based cathode for highly reversible lithium-sulfur batteries, ChemSusChem 7 (2014) 1265–1273, https://doi.org/10.1002/cssc.201300782.
[62] R. Pongilat, S. Franger, K. Nallathamby, Functionalized carbon as polysulfide traps for advanced lithium-sulfur batteries, J. Phys. Chem. C. 122 (2018) 5948–5955, https://doi.org/10.1021/acs.jpcc.8b00605.
[63] G. Zheng, Q. Zhang, J.J. Cha, Y. Yang, W. Li, Z.W. Seh, Y. Cui, Amphiphilic surface modification of hollow carbon nanofibers for improved cycle life of lithium sulfur batteries, Nano Lett. 13 (2013) 1265–1270, https://doi.org/10.1021/nl304795g.
[64] R. Fang, C. Liang, Y. Xia, Z. Xiao, H. Huang, Y. Gan, J. Zhang, X. Tao, W. Zhang, Supercritical CO2 mediated incorporation of sulfur into carbon matrix as cathode materials towards high-performance lithium-sulfur batteries, J. Mater. Chem. A Mater. 6 (2017) 212–222, https://doi.org/10.1039/c7ta08768c.
[65] Y. Zhu, W. Zhao, X. Ye, Supercritical CO2-assisted fabrication of CeO2 decorated porous carbon/sulfur composites for high-performance lithium sulfur batteries, SN Appl. Sci. 1 (2019) 471, https://doi.org/10.1007/s42452-019-0492-6.
[66] J. Zhao, L. Zhang, X. Li, X. Tao, W. Zhu, X. Ye, Supercritical CO2 assisted fabrication of activated carbon-sulfur composite for improved lithium-sulfur batteries, J. Alloy. Compd. 708 (2017) 264–269, https://doi.org/10.1016/j.jallcom.2017.02.289.
[67] Y. Xia, H. Zhong, R. Fang, C. Liang, Z. Xiao, H. Huang, Y. Gan, J. Zhang, X. Tao, W. Zhang, Biomass derived Ni(OH)2@porous carbon/sulfur composites synthesized by a novel sulfur impregnation strategy based on supercritical CO2 technology for advanced Li-S batteries, J. Power Sources 378 (2018) 73–80, https://doi.org/10.1016/j.jpowsour.2017.12.025.